2014-01-01

Electronic Structure And Charge Transfer Excited States Of Endohedral Fullerene Containing Electron Donor-Acceptor Complexes Utilized In Organic Photovoltaics

Fatemeh Amerikheirabadi
University of Texas at El Paso, famerikheirabadi@miners.utep.edu

ELECTRONIC STRUCTURE AND CHARGE TRANSFER EXCITED STATES OF ENDOHEDRAL FULLERENE CONTAINING ELECTRON DONOR-ACCEPTOR COMPLEXES UTILIZED IN ORGANIC PHOTOVOLTAICS

FATEMEH AMERIKHEIRABADI

Department of Physics

APPROVED:

Rajendra R. Zope, Ph.D., Chair

Tunna Baruah , Ph.D.

Carl W. Dirk, Ph.D.

Charles Ambler, Ph.D.
Dean of the Graduate School

Dedication

To my Family

ELECTRONIC STRUCTURE AND CHARGE TRANSFER EXCITED STATES OF ENDOHEDRAL FULLERENE CONTAINING ELECTRON DONOR-ACCEPTOR COMPLEXES UTILIZED IN ORGANIC PHOTOVOLTAICS

by

Fatemeh Amerikheirabadi, BSc

THESIS

Presented to the Faculty of the Graduate School of

The University of Texas at El Paso

in Partial Fulfillment

of the Requirements

for the Degree of

MASTER OF SCIENCE

Department of Physics

THE UNIVERSITY OF TEXAS AT EL PASO

August 2014

Acknowledgements

I would like to appreciate, from the bottom of my heart, my family especially my dear parents who have always been supporting me. I would also like to thank my mentor Dr. Rajendra R. Zope as well as Dr. Tunna Baruah who as a member of their active group, I found the opportunity of growing as a researcher and learning how to get well-equipped in order to do a fruitful job in the science world. I am also deeply grateful to Dr. Luis Basurto who had a big role in learning the computational part of this work and who answered my questions patiently and thoroughly. I am also thankful to Dr. Carl W. Dirk who, provided a very short time, examined this document very carefully and made valuable recommendations. Finally, I acknowledge the Couri student research assistant program which as a funding source helped me to allocate my time fully to conducting this research work.

Abstract

Organic Donor-Acceptor complexes form the main component of the organic photovoltaic devices (OPVs). The open circuit voltage of OPVs is directly related to the charge transfer excited state energies of these complexes. Currently a large number of different molecular complexes are being tested for their efficiency in photovoltaic devices. In this work, density functional theory as implemented in the NRLMOL code is used to investigate the electronic structure and related properties of these donor-acceptor complexes. The charge transfer excitation energies are calculated using the perturbative delta self-consistent field method recently developed in our group as the standard time dependent density functional approaches fail to accurately provide them. The model photovoltaics systems analyzed are as follows: $Sc_3N@C_{80}$_ZnTPP, $Y_3N@C_{80}$_ZnTPP and $Sc_3N@C_{80}$_ZnPc. In addition, a thorough analysis of the isolated donor and acceptor molecules is also provided. The studied acceptors are chosen from a class of fullerenes named trimetallic nitride endohedral fullerenes. These molecules have shown to possess advantages as acceptors such as long lifetimes of the charge-separated states.

Table of Contents

List of Tables

List of Figures

Chapter 1: Introduction

The basic idea behind the conducted and presented research is to contribute in the extensive efforts that are being made with the aim of finding promising alternative energy resources in order to alleviate our currently intense dependence on fossil fuel reserves.

The vital role of energy in our everyday life is an unquestionable fact. On the other hand, it is manifestly clear that we cannot rely on the conventional non-renewable energy resources meaning fossil fuels, anymore. Not only they cannot meet our growing energy demands but also the subsequent disastrous effects of their over consumptions are unavoidable. So far, various types of substitutes have been introduced and put into practice. However, the idea of employing solar energy appears to be more tempting due to its vast advantages such as being a free, clean and ample reserve. The annual energy that earth receives from sun (5% UV, 43% visible, 52% IR) goes beyond the world's yearly energy use by several thousand times (1).

A solar cell also called a photovoltaic (PV) cell is any device that converts solar radiation directly into electricity using photovoltaic effect (creation of voltage in a material due to exposure to light). This effect was first observed by a French physicist named A.E. Becquerel in 1839 (2) which can be claimed to be one of the very first sparkles of the construction of today's solar cells.

Based on the materials utilized in their architecture, PVs are classified into two main categories, inorganic and organic cells. Herein, a brief introduction to inorganic photovoltaics (IPVs) will be presented. In the next chapter, the organic photovoltaics (OPVs) will be discussed in details along with a comparison of the both kinds.

The first solid-state solar cell was fabricated by C. Fritts in 1883. It was composed of a thin layer of Au deposited on Se semiconductor (2,3) which worked as the light absorber in order

to generate electron-hole pairs from incident photons. Free charge carriers were then created as the electron-hole pairs were separated by the electric field presented in the Au/Se schottky junction. Photon absorption and charge separation are still the two fundamental phenomena of the inorganic solar cell's function (3). The current inorganic photovoltaics were originally established at Bell laboratories employing a single-crystal Si wafer and a p-n junction for light absorption and charge separation, respectively (3,4). In general, the inorganic materials applied to produce inorganic solar cells include crystalline, multicrystalline, amorphous and microcrystalline Si, the III-V compounds and alloys, CdTe and the chalcopyrite compound. Crystalline and multicrystalline solar cells are the most commercially produced cells (5).

Figure 1, demonstrates the energy conversion efficiency progress of different solar cell technologies over the last four decades. The energy conversion efficiency of a solar cell is the percentage of the solar energy to which the cell is exposed that is converted into electrical energy (2). The graph shown in figure 1 was reported on June 27, 2014 by US department of energy (National Renewable Energy Laboratory) (2). The so-called multijunction cells hold the efficiency record at 44.7% among all the other photovoltaic technologies. In this kind of cell, two, three or four junctions are used and each junction having a different band gap is responsible for absorbing sun light in a certain region of solar spectrum and its high efficiency may be attributed to this feature. The efficiency of monocrystalline solar cells has reached 27.6% while that of multicrystalline cells is 20.4%. The reported efficiency for organic solar cells shows the value 11.1%.

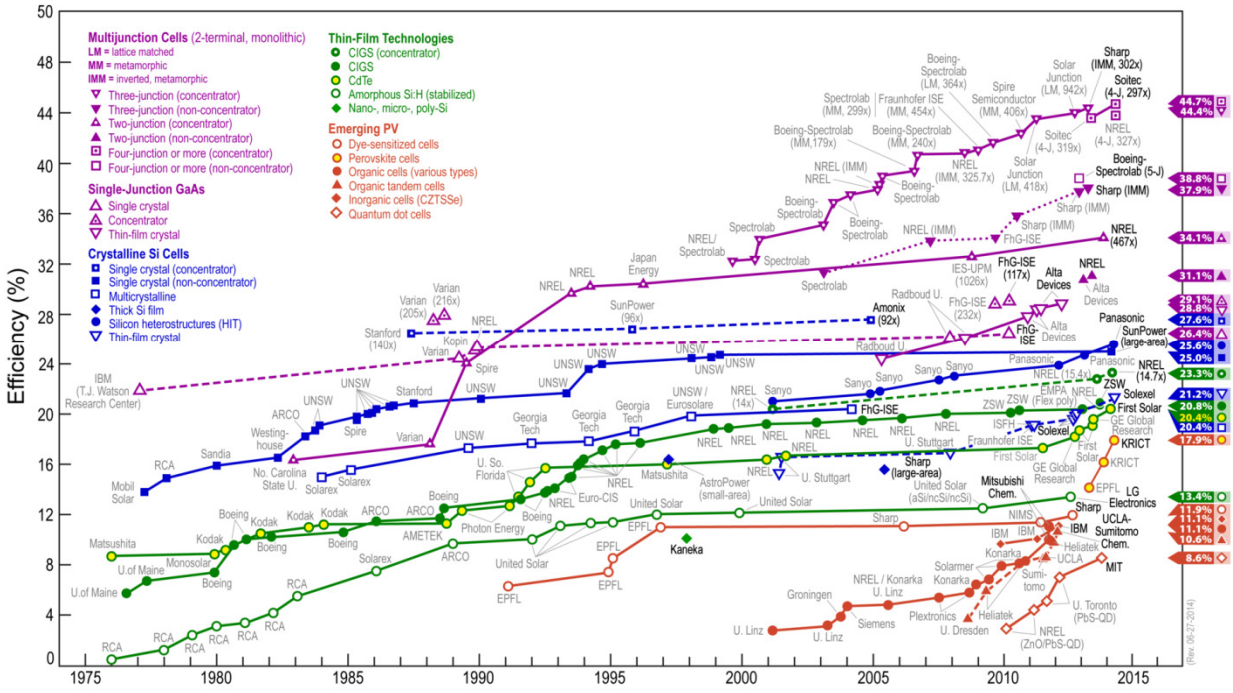

Figure 1. The energy conversion efficiency progress of the different solar cell technologies over the last four decades, reported on June 27, 2014 by US department of energy (National Renewable Energy Laboratory) (2).

However, Hybrid photovoltaic devices which are a combination of IPVs and OPVs exhibit higher efficiencies compared to individual I/O PVs. This type of PVs as well as their advantages will be discussed shortly in the next chapter. In addition, throughout the next chapter, a thorough investigation into the organic photovoltaic devices from the fundamental process underlying the device function to the different influential factors that their variation can play an essential role in improving the overall efficiency of these devices will be presented.

Chapter 3 describes the computational methods employed in order to calculate different physical properties for the studied systems. In chapter 4, the outcome of the calculations carried out on the isolated so-called donor (D) and acceptor (A) components, which have been applied in this work, are presented and examined thoroughly.

Chapters 5 and 6 contain the results of the performed calculations on three different electron donor-acceptor dyads along with a complete analysis of the acquired data. The properties calculated include adiabatic/vertical ionization potentials and electron affinities, charge transfer excitation energies, orbital electron densities, ground state density of states, etc. In the 5th chapter, the obtained results of different calculations performed on two isomers of the molecule $Sc_3N@C_{80}$-ZnTPP (Zinc TetraPhenyl Porphyrin) will be fully reported and studied. In the 6th chapter, $Y_3N@C_{80}$-ZnTPP and $Sc_3N@C_{80}$_ZnPc complexes will be probed. In this chapter the three dyads will be compared. The goal is to study the effect of changing the donor or the acceptor component on ground state and excited state electronic structure of the $Sc_3N@C_{80}$_ZnTPP construct.

The complexes analyzed here, have employed endohedral metallofullerenes ($Sc_3N@C_{80}$ and $Y_3N@C_{80}$) as the acceptor part. These are fullerenes that host additional atoms, ions or clusters within their inner spheres. They exhibit extraordinary features that make them super candidates for utilization in solar cells. In the second chapter, the advantages of applying endohedral metallofullerenes as the acceptor component of the donor-acceptor complexes are discussed thoroughly.

Furthermore, the applied donors (ZnTPP and ZnPc) have already proved their positive influence on improving the efficiency of OPVs and have played an essential role in understanding the function of these devices.

Finally, in order to identify the most promising donor and acceptor candidates which form the basic component of OPVs, a broader and more targeted series of interdisciplinary research is essential. Continuous integrated attempts and collaborations of scientists in this field may eventually bring about overcoming the current energy crisis.

Chapter 2: Background

Organic Photovoltaic devices (OPVs) have attracted a great deal of attention over the last few decades simply due to their unique properties. A large-area plastic photovoltaic device can be fabricated at a low cost; in addition organic materials have low specific weight and demonstrate a good mechanical and chemical flexibility and a nearly unlimited variability (1,6,7). Another outstanding feature is their high optical absorption coefficients (as high as 10^5 cm^{-1}) (8) compared with inorganic based cells (9). These are desirable characteristics for an ideal solar cell.

In 1977, it was discovered that the conductivity of carbon-based molecular and polymeric materials can be promoted by several orders of magnitude upon chemical doping. Until then, these types of materials were considered as electrical insulators (9). In most cases, a p-type (n-type) semiconductors' conductivity can be boosted by chemical doping with n-type (p-type) materials (1). This discovery caused a swiftly growing field of research into these materials. The unique electronic properties of these semiconductors are connected to their conjugated chemical structures. It means that the bonds between carbon atoms are alternating single or double (called conjugation) (9).

The HOMO (Highest Occupied Molecular Orbital)-LUMO (Lowest Unoccupied Molecular Orbital) energy gap in these materials ranges from 1 to 4 eV which makes them ideal candidates for the purpose of utilization in optoelectronic devices working in the visible region of the electromagnetic spectrum (9).

An organic solar cell is composed of an active layer sandwiched between two electrodes with different work functions. The electrode which is exposed to the sunlight is (semi)

transparent. The photoactive layer, which concerns our research, can be based on a single, a bi-layer (planar heterojunction) or a blend of two (or more) semiconductors (bulk heterojunction) (9). Figure 2, pictures the structure of the last two mentioned types of solar cells. ITO (Indium Tin Oxide) electrodes are typically used as the first layer because they are conductive and transparent (transmitting about 80 % of the sun rays lying in the visible region of solar spectrum) (1,8).

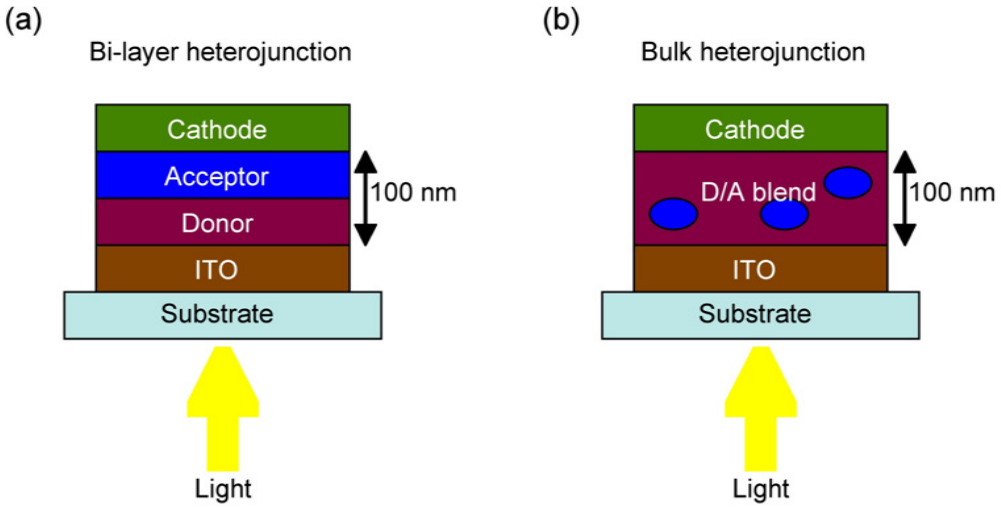

Figure 2. The structure of the two different types of organic solar cells. (a) Bi-layer heterojunction, and (b) Bulk heterojunction.

As displayed, in bilayer cells, two organic layers with particular hole or electron transporting characteristics respectively called donor and acceptor layers are deposited directly over one another with a planar interface. The two electrodes match the donor HOMO and acceptor LUMO (7). It has been found that only 10 % of the thickness of these layers will be

involved in electron transfer. On the other hand, in bulk heterojunction cells a mixture of donor and acceptor materials form the active layer. Thus, donor-acceptor interfacial area increases which boosts electron transfer (10). That is why bulk heterojunction devices are more efficient.

Thin film OPVs can be produced either by vacuum evaporation/sublimation or solution processing techniques (8) based on their building blocks. Thermal stability is desired for evaporation whereas solubility is essential for solution processing. Small molecules are almost always more soluble than polymers. Thermal stability is complex, and is usually not strongly related to the size of the molecule/polymer. Solubility can be modified by adding solubilizing groups (8). Polymer-based solar cells are solution processed at low temperatures since their huge molar mass prevents their evaporation and they decompose if overheated (7,8).

The power conversion efficiency (PCE, η) of OPVs depends on four parameters, open circuit voltage (V_{oc}), short circuit current (I_{sc}), Fill Factor (FF) and incident light power density (P_{in}). PCE is given by the following formula (8):

$$\eta = (V_{oc} * I_{sc} * FF)/ P_{in}$$

The photovoltage (in volts) developed while the terminals are open is called the open circuit voltage. In general, in a metal-insulator-metal device, V_{oc} is correlated to the work functions' difference of the two metals (8,11). On the other hand, in a p-n junction, the maximum available voltage is given by the difference between the quasi Fermi levels of the two charge carriers (n-doped and p-doped semiconductors' energy levels). In OPVs, the open circuit voltage is linearly dependent on the HOMO of the donor (quasi Fermi level of the p-type semiconductor) and LUMO of the acceptor (quasi Fermi level of the n-type semiconductor) (8,12). Brabec et al.

demonstrated the linear relation between the first reduction potential (LUMO level) of the (fullerene) acceptors and the obtained V_{oc} (8,12) and Scharber et al. reported the linear correlation between the first oxidation potential (HOMO level) of the donors and the V_{oc} (8). Therefore, V_{oc} is a sensitive function of the donor-acceptor's energy levels and identifying proper donor-acceptor pairs resulting in higher V_{oc} is an active field of research (13).

The short circuit current (in amperes) is the current through the solar cell when it is short circuited (i.e., when the voltage across the cell is zero). It is directly related to the photoinduced charge carrier density and charge carrier mobility in the organic semiconductor. The latter is a device parameter not a material parameter and is sensitive to the nanomorphology of the active layer (8) which in turn depends on the film preparation details. As a result, although a bulk heterojunction device enhances the contact surface between the donor and acceptor components, its complex nanomorphology makes it difficult to control and optimize the active layer (8).

The Fill Factor is the ratio of the actual maximum obtainable power to the product of the open circuit voltage and short circuit current (2). It is tied to the number of charge carriers reaching the electrodes. Basically, the charge carrier recombination and transport are two competing events and to achieve a high Fill Factor, the product of the lifetime of the charge carriers and their mobilities, which determines the distance that they can travel in a given electric field, has to be maximized (8).

The foundational mechanism taking place in a donor-acceptor based organic photovoltaic device, the photoinduced charge transfer process, can be explained in a few steps as displayed schematically in figure 3.

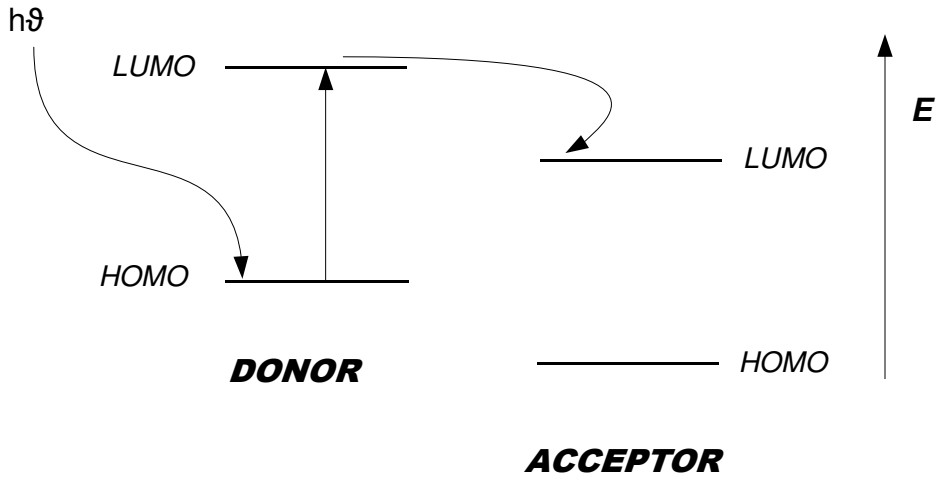

Figure 3. The fundamental mechanism occurring in a donor-acceptor based organic photovoltaic device. HOMO stands for the Highest Occupied Molecular Orbital and LUMO stands for the Lowest Unoccupied Molecular Orbital.

A light's particle (photon) strikes the donor molecule and if absorbed, makes an electron transfer from its HOMO to the LUMO level, resulting in a coulombically bound particle-hole pair called exciton.

Excitons are quasi particles that engender new states within the forbidden band gap and are detectable through optical transitions with known energies (6). There are two types of excitons based on their delocalization, Frenkel excitons if they are localized and Mott-Wannier excitons if they are delocalized, i.e. if they extend over many molecular components. Furthermore, based on the spin of the electron and the hole constructing the exciton, one can distinguish two types of excitons. If both of the electron and the hole have the same spins, it is called a triplet exciton and if the electron and the hole have opposite spins, then it is named a singlet exciton as demonstrated in figure 4.

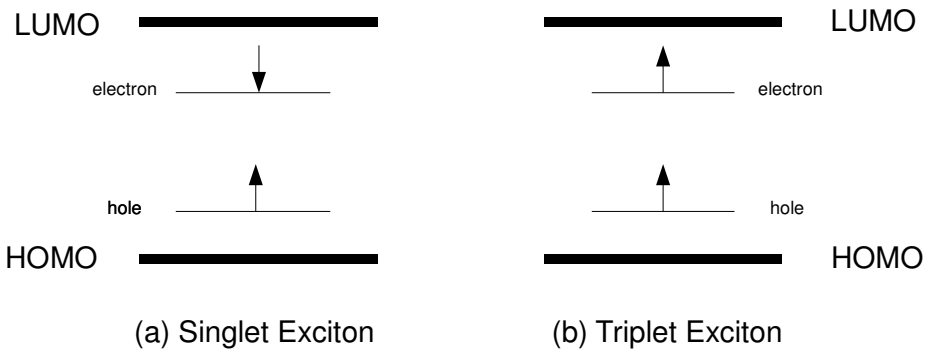

Figure 4. Different types of excitons based on the spins of the electron and the hole. (a) Singlet exciton, and (b) Triplet exciton.

At this step, the donor part of the complex is said to be locally excited. However, because it is energetically favorable for the photoexcited electron, and also due to the high electron affinity of the acceptor component, the excited electron moves to the LUMO energy level of the acceptor molecule while it is still coulombically bound to the hole, giving rise to an excitation delocalization on donor-acceptor complex. At this step, the charge transfer initiates and after formation of ion radical pairs (ions that have unpaired valence electrons), the electron will be transferred to the acceptor (6).

In general, it is evaluated that only 10% of the photoexcitations give rise to free charge carriers in conjugated polymers (8). It is partly attributed to the exciton dissociation. In order for the exciton dissociation to occur efficiently, strong electric fields are required. These fields can be supplied either externally or through interfaces due to their different work functions. Thus, the exciton generation must occur in the close proximity to the donor-acceptor interface, within the exciton diffusion length (average distance that an exciton can diffuse through a material before its annihilation due to recombination) or else it will decay without any contribution to the

electrical current. In fact, this condition imposes a limit on the thickness of the active layer, considering that the typical diffusion lengths are around 10-20 nm (8,9). However, the thickness of the active layer in most of these devices ought to be above 100 nm in order to absorb maximum light while only a small fraction of the excitons makes it to reach the interface and dissociate. As mentioned earlier, the bulk heterojunction cells alleviate this problem to a great degree by mixing the donor and acceptor which increases the interfacial area and reduces the distance that excitons need to travel to reach the interface (9).

Finally, the created free charge carriers ought to be transported to the appropriate collecting electrodes within their lifetime, that is, before recombination. The required driving force is supplied by the gradient in the chemical potentials of electrons and holes (quasi Fermi levels of the doped phases) created in the donor-acceptor junction. This gradient is determined by the difference between the HOMO level of the donor (quasi Fermi level of the holes) and LUMO level of the acceptor (quasi Fermi level of the electrons). This internal electric field (E=-gradient U) not only contributes to the drift of charge carriers but also determines the maximum open circuit voltage (V_{oc}) of OPVs, as mentioned earlier (8). It is crucial to mention that at each intervening step, the process may settle back to the ground state by dissipating energy in heat form or via electromagnetic radiation (6). For the sake of recombination reduction, the electrons and holes are transported in different types of materials. For instance, in our case (donor-acceptor based OPVs) a proper electron conductor is applied as the acceptor (an n-type semiconductor with a large electron affinity) and a good hole conductor is used as the donor (a p-type semiconductor with a low ionization potential).

This simple scheme of the photogenerated charge transfer event can be summarized as follows, where D and A denote Donor and Acceptor, respectively.

i. $D+A \rightarrow D^*+A$ Donor Excitation

ii. $D^*+A \rightarrow (D–A)^*$ Excitation delocalization on D-A Complex

iii. $(D–A)^* \rightarrow (D^{\delta+}\_A^{\delta-})^*$ Charge transfer initiation

iv. $(D^{\delta+}\_A^{\delta-})^* \rightarrow (D^{+\bullet}\_A^{-\bullet})$ Ion Radical pair formation

v. $(D^{+\bullet}\_A^{-\bullet}) \rightarrow D^{+\bullet}+A^{-\bullet}$ Charge separation

δ shows the fraction of the transferred charge, ranging from 0 to 1. As it gets 1, the whole electron has been transferred (6).

A distinctive feature of the charge transfer process in D-A constructs is that the orbitals contributing in the electron transfer are spatially well separated with vanishing overlap (14).

In principle, only a small fraction of the incident solar irradiation is harvested by organic materials due to their large band gap (8). Therefore, materials possessing lower band gaps are desired to be utilized as the donor molecule (7,8). In addition, in order to increase the probability of photon absorption by the device at the very first step or in other words to expand the range of the incident photons' wavelengths that lead to excitation, one way is to attach some additive antenna systems to the donor. Each of these antenna chromophores possesses high absorption coefficients in a certain range of wavelengths different from the others and therefore a wide range of wavelengths will be covered by the donor molecule. There should be a fast energy transfer among the chromophores in order to compete with the excited states' relaxation by other

processes like fluorescence. Two factors affecting the energy transfer are the distance between any two chromophores and their relative orientation. Antenna systems also add control and photoprotective mechanisms, a legacy of natural photosynthesis, to the system (15). Evidently, a higher photon absorption rate can be directly proportional to a higher efficiency for the cell. An example of a system using this mechanism is the macromolecule heptad, depicted in figure 5.

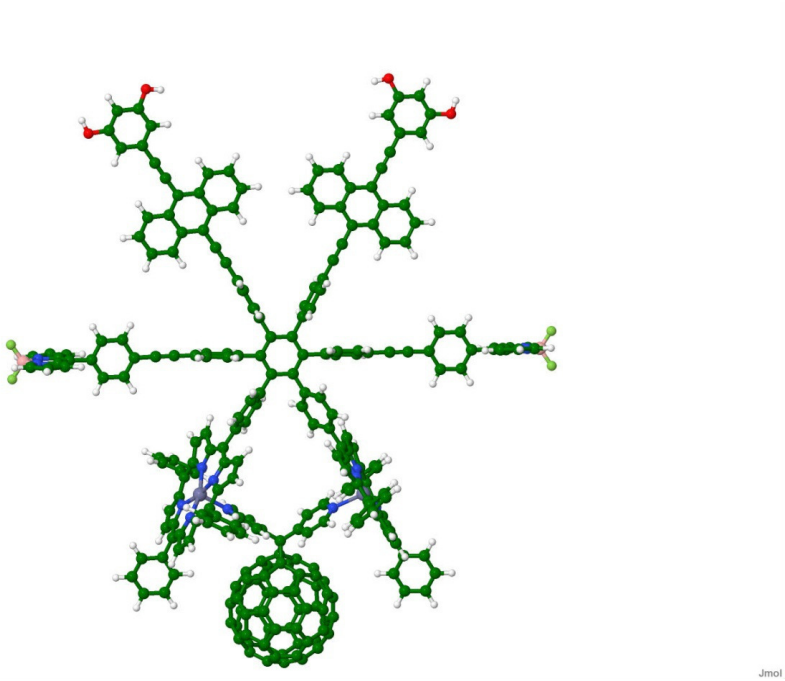

Figure 5. A picture of the macromolecule heptad. This molecule, having several antenna systems, can absorb photons with a wide range of wavelengths.

There is also a type of PVs called concentrating photovoltaics (CPV) which uses the idea of concentrating sunlight by means of optical devices such as mirrors or lenses. It gives rise to higher efficiencies and reduces the area of the cells (9).

The energy-band structure of the organic materials is much more complex than the inorganic crystalline or amorphous semiconductors (1) and this brings about fundamental differences between their properties. The organic semiconductors can be classified as "intrinsic wide band gap materials" with a low intrinsic charge carrier density at room temperature in the dark. However, introduction of extrinsic charge carriers into them through chemical, photochemical or electrochemical doping can be applied to boost their electrical conductivity (8).

It is well documented that the lower power conversion efficiency of OPVs compared with that of their IPV counterparts is essentially attributed to the lower photogeneration efficiency of mobile charge carriers and the higher electrical resistivity of the organic materials which is due to the low density and mobility of the charge carriers (7). Furthermore, excitons' diffusion lengths are relatively small in OPVs compared with IPVs' which is a consequence of stronger exciton binding energies in these devices (7).

Charge–separated state stabilization and huge charge carrier mobilities are principal factors in producing an efficient solar cell. To reach the first factor, three component systems (triads) have been introduced and synthesized (15). One example of such systems is the Carotenoid (C)-Porphyrin (P)-Fullerene (C_{60}) system. Figure 6, displays the structure of CPC_{60}. In this macromolecule, after the formation of $C\text{-}P^{\bullet+}\text{-}C_{60}^{\bullet-}$, the positive charge will rapidly be shifted to the carotene fragment as the carotenoid donates an electron to the positively charged porphyrin, yielding $C^{\bullet+}\text{-}P\text{-}C_{60}^{\bullet-}$. The lifetime of this charge-separated state is reported to be about hundreds of nanoseconds while displaying a large dipole moment of about 153 D (16). At this state, since the charges are spatially well-separated, the charge recombination process will be slower (15,17).

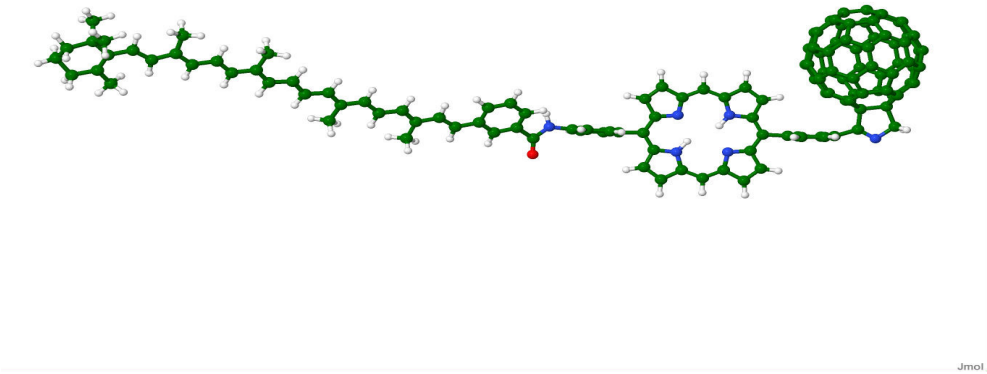

Figure 6. A picture of the macromolecule CPC_{60}. This molecule, employing two donors, makes the charge recombination process slower.

Experimental evidence states that the V_{oc} of OPVs, which is one of the determining factors in power conversion efficiency (PCE) of these devices, is directly related to the photo-induced charge-transfer (CT) excited state energies (14,18). It has been found that CT excitation energies depend thoroughly on the ground-state properties of the separated systems (16). The lowest CT excitation energies can be approximately calculated using the following formula known as Mulliken's equation:

$$E_{ex}=IP_{(donor)} - EA_{(acceptor)} - 1/R$$

where IP and EA denote the ionization potential of the donor and electron affinity of the acceptor component, respectively and R gives the hole-electron separation (19,20). The 1/R term is the coulomb energy originating from the electrostatic interaction between the charged donor and

acceptor species. It is commonly calculated using partial charges on donor-acceptors in the coulomb energy expression (13).

One of the factors influencing the charge transfer energetics of the complexes is the relative orientations of the donor and acceptor components which can be placed either in a co-facial or an end-on configuration. These variations create different associated local electric fields which make a shift in the frontier orbital energy levels influencing the exciton dissociation at the D-A interface. The two mentioned orientations are depicted in figure 7. The surface-to-surface interaction of the D-A is largest in co-facial alignment (14). The polarization effects arising from the interaction of the D-A charge distributions, which change the energy levels, are decreased in going from co-facial to end-on orientation (13,14). Likewise, the strength of the non-covalent pi-pi interactions is decreased in end-on geometry compared to those in co-facial alignment. As a result, the CT excitation energies are larger for the end-on geometry than the co-facial structure due to a lower exciton binding energy in end-on orientation (14). Practically, in the active layer of OPV cells a combination of different orientations may co-exist (13,14). However, all the dyads studied in this work are in co-facial position.

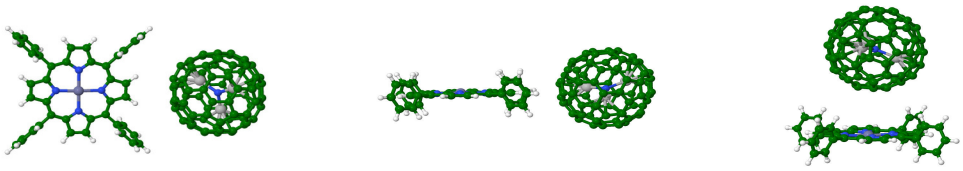

Figure 7. Relative orientations of the donor and acceptor components with respect to each other are shown. The first two in the left side show two different views of the end-on orientation and the right side structure displays the co-facial orientation.

Another influential element in the CT energies is the distance between the donor and acceptor parts; however, its effect is less than the relative D-A orientations (14).

Our study is focused on a single donor-acceptor pair; however, in a real solar cell many of them are placed together which brings along the influence of their interactions on the energy levels of each other and subsequently, changes the overall properties of the cell. It is also necessary to mention that all the calculations executed in this work are in gas phase, although in practice the molecules under investigation may be placed in a solvent such as toluene, chloroform or benzonitrile which in turn will directly affect the results. For instance, in bulk heterojunction devices, the final morphology of the active layer depends substantially on the particular solvent used (7). Furthermore, it has been indicated that the solvent polarization, especially in polar solvents, generates a reaction electric field which in turn affects the reordering of the excited states and thus subsequently, the charge-separation process (14,16). It is possible to mimic the solvation effects in the calculations using our code by means of charge embedding schemes. However, solvents effects were not investigated due to time constraints.

The ground state dipole moment of a supramolecular D-A pair demonstrates the formation of interfacial dipoles, which can be useful in orbital alignments in such a way that leads to better exciton dissociation (14,21). The dipole can be due to ground state charge transfer from the donor to acceptor or solely due to the polarization effects. The ground state charge transfer reduces as the D-A components get farther away and makes the polarization effect entirely responsible for the dipole formation at large separations (20).

To make use of the unique properties of both organic and inorganic materials hybrid photovoltaic devices were introduced (8). In this type of cells, an organic material serving as the

hole conductor is mixed with a good electron transporting inorganic material in order to benefit from the particular features of both types of materials. A practical method for the fabrication of Hybrid cells is to combine inorganic nanocrystals with semiconductive polymers in a bulk heterojunction structure. The excitons' dissociation into free charge carriers happens efficiently at interfaces of inorganic semiconductor nanoparticles and organic semiconductors. Some of the advantages of this type of Hybrid solar cells are as follows:

1. The band gap of inorganic nanoparticles can be tuned by changing their size. Thus, their absorption/emission spectra can be controlled.

2. The inorganic materials possess higher photoconductivity compared with most of organic semiconductors.

3. Nanoparticles can be synthesized to act either as a p-type or n-type semiconductor.

However, some of the challenges are the instability of the nanoparticles and different solubility characters of the organic and inorganic components (8).

In the following section the advantages of applying endohedral metallofullerenes are explicated.

2.1 ENDOHEDRAL METALLOFULLERENES AND ADVANTAGES OF THEIR UTILIZATION

Fullerenes are the molecules totally composed of carbon atoms, in the form of empty spheres, ellipsoids or tubes. They emulate some of the features of natural light harvesting systems and this is one of the reasons for their employment in OPV devices. In addition, they have rigid structures and show small reorganization energies during charge transfer reactions (22). The most abundant fullerene is the so-called buckyball molecule, C_{60}. It can accept up to

six electrons and this ability renders it as a good candidate to be used in photoinduced charge transfer systems but it also has a disadvantage; it is insoluble. This deficiency led to the employment of PCBM (Phenyl C_{61} Butyric acid Methyl ester) which is a soluble derivative of C_{60}. However, chemical modifications of fullerenes can alter or enhance their electrical, chemical and optical properties such as solubility, stability, absorption and color (6).

Endohedral fullerenes, fullerenes hosting extra atoms, ions or clusters in their spheres, have become particularly attractive due to the possibility of a vast control over their chemical and physical properties by just changing the nature and composition of the encapsulated units (22). In these endohedral fullerenes, the size of the carbon cage can be small like in $U@C_{28}$ or quite large like in $La@C_{106}$ (23). Endohedral metallofullerenes (fullerenes containing metals), in particular, have become one of the most appealing research areas because of their outstanding characteristics. They display an excellent stability under ambient conditions although in some cases neither the empty cage nor the encapsulated unit exists in isolation (24). Furthermore, since the HOMO-LUMO gap is a function of the encapsulated unit, cage size, symmetry and exohedral functionalization, the energy band gap can easily be tuned for a wide range of applications (25). For instance, the endohedral fullerenes have demonstrated a great potential for biomedicine and nanomaterials sciences' related applications (24,26). However, the exploration of their physical and chemical properties has been restricted due to difficulty in their preparation and isolation in large quantities. In 1999, a remarkable progress took place when Dorn and co-workers reported the synthesis of trimetallic nitride endohedral metallofullerenes (TNEFs) for the first time using a method called trimetallic nitride template (TNT) (24). In this process, nitrogen gas is introduced into the Kratschmer-Haffman generator while packed graphite rods containing metal oxides are vaporized (27). This method has facilitated producing macroscopic quantities of

molecules such as $Sc_3N@C_{80}$ (24). Endohedral fullerenes entrapping metallic carbides, metallic oxides and metallic sulfides as well as mixed nitride/carbides are also known. The isolated-pentagon rule (IPR) (according to this rule, all the pentagons in a fullerene cage are surrounded by hexagons to mitigate the strain produced when two pentagon rings are fused) obeying empty fullerene structures, without any exception, are the most stable cages. However, it does not apply to endohedral metallofullerenes, since several non-IPR cages have been isolated (25). The two most stable C_{80} empty cages out of its seven possible structural isomers are the ones with D_2 and D_{5d} symmetries. It is interesting to mention that the two least stable empty cage isomers with I_h and D_{5h} symmetries become extensively prevalent as the cages incarcerate the metallic nitride clusters. The investigation of the electronic properties of this class of compounds suggests a charge transfer from the encapsulated moiety to the fullerene cage (24). The Nagase and Akasaka groups have shown the strong electron-accepting character of monometallofullerenes ($La@C_{82}$,$Gd@C_{82}$) and dimetallofullerenes ($La_2@C_{80}$, $Sc_2@C_{84}$) as well as proving that the reactivity depends on whether an endohedral metal unit exists in the carbon cage or not, although; the nature of the metal inside the cage does not affect the reactivity. A different result was observed for trimetallic nitride endohedral fullerenes. An intense dependency on the nature of the incarcerated metal was observed for the reactivity of the molecule, $Sc_3N@C_{80}$ and $Y_3N@C_{80}$ showed a dramatically different reactivity toward exohedral chemical functionalization (24). It has been shown that the lifetime of the charge-separated states (typically nanoseconds (28)) using the metallofullerenes can be of the order of microseconds (μs) (22). One of the limitations of the OPV device power conversion efficiencies (PCEs) is the low voltage output due to a molecular orbital mismatch between the donor and the acceptor. On the other hand, as mentioned earlier, the open circuit voltage in such devices is directly correlated to

the difference between the HOMO level of the donor and LUMO level of the acceptor (2). Based on the experimental and theoretical data, the LUMO levels of TNEFs are much higher (with respect to Fermi level) than those of empty-cage species and it opens a new window towards higher V_{oc} and thus higher efficiencies for OPVs (29). To sum up, using TNEFs reduces the molecular orbital mismatch and the energy loss during charge transfer state and increases the V_{oc}. The difference between the energy levels of TNEFs and empty-cage fullerenes is illustrated in figure 8.

Endohedral metallofullerenes have greater absorption coefficients than empty cage fullerenes like C_{60} in the visible part of the electromagnetic spectrum and a lower HOMO-LUMO gap while showing a similarly noticeable electron-accepting ability (26).

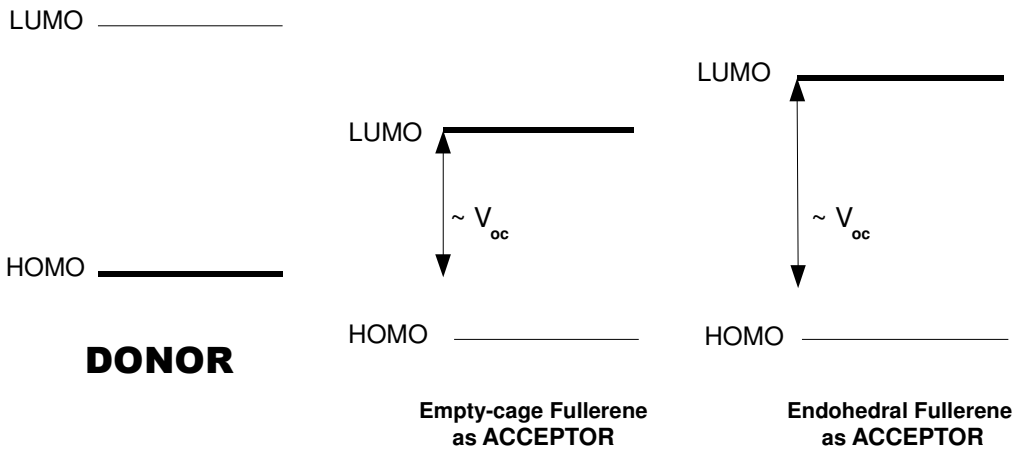

Figure 8. Comparing the obtained open circuit voltages in OPV devices that apply empty-cage fullerenes or trimetallic nitride endohedral fullerenes as acceptors. The positive effect of endohedral fullerenes is clearly demonstrated.

Comparing the redox potentials of $M_3N@C_{80}$ (M=Sc, Y, Lu, Pr) reveals the cluster-dependent electrochemical character of these compounds. Therefore, the electron-accepting

feature of these molecules can be tuned just by changing the nature of the metal cluster inside the cage (30).

The electrochemical behaviors of endohedral metallofullerenes differ from those of empty fullerenes. For example, the one electron oxidation of $M_3N@C_{80}$ (M=Sc, Y, La) is a lot easier than that of empty fullerenes, while its one-electron reduction may occur at any lower or higher redox potential with respect to empty cages. Hence, from the electrochemical standpoint, endohedral metallofullerenes can be employed either as a donor or as an acceptor. In 2012, Feng and colleagues used a trimetallic nitride endohedral fullerene ($Lu_3N@C_{80}$) as a donor in a donor-acceptor conjugate where Perylenebisimide (PDI) played the role of acceptor as well as light harvester. The photophysical studies indicated a photogenerated charge transfer from $Lu_3N@C_{80}$ to PDI giving rise to the creation of an stable radical ion pair $(Lu_3N@C_{80})^{+\bullet}$ — $(PDI)^{-\bullet}$ with a lifetime of about 120 picoseconds in toluene. This verifies the dual electron-donor/electron-acceptor character of the nitride clusterfullerenes; however, the corresponding short radical ion pair lifetime of these complexes hampers their practical use (30).

Both the acceptors used in this work, $Sc_3N@C_{80}$ and $Y_3N@C_{80}$ are endohedral metallofullerenes.

Chapter 3: Computational methods

The dyads studied in this work are classified as the supramolecular systems and because of their huge size (141, 161 atoms), the quantum chemical methods such as configuration interaction (CI) or multireference CI cannot be applied to compute their excited states due to large size of the systems. The density functional theory (DFT) based calculations have had a key role in dissecting the materials' properties as well as in searching for new materials. In DFT method, the ground state electron density plays the central role. The excited state study of the systems containing around one hundred atoms is usually done using the time dependent density functional theory (TDDFT) particularly in its linear response formulation. In fact, TDDFT method has been the main tool for calculating the excited states and optical spectra of a broad range of systems. However, it cannot be used in determination of the donor-acceptor conjugates' excitation energies due to failure to describe the charge transfer excitations unless some system dependent tricks are used (13). Thus, some research groups use a constrained formalism of DFT, in which a constraint is applied to describe the lowest charge transfer excitation energies of these complexes. This approach establishes a constraining potential to enforce electron density's localization (20,31). This approach provides only the lowest excited states. Our group has recently developed a method that allows efficient calculations of the electronic excitations. This method is a variant of the delta self-consistent method and employs perturbation theory to compute the excited states. In this method, an orthogonality constraint between the ground state and excited state Slater determinantal wave functions is maintained. So any excitations, not just the lowest charge transfer excitations can be calculated. The benchmark calculations of the method on a set of TCNE-hydrocarbon along with realistic models of donor-acceptor complex showed that the method can accurately describe charge transfer excitations (13,16). This

approach is implemented in NRLMOL (Naval Research Laboratory Molecular Orbital Library) code which is an extensively parallel code designed for electronic structure calculations of large molecules and clusters. With NRLMOL, molecular properties such as electronic structure, density of states, optimized geometry, bond lengths, dipole moment, spin magnetic moment, harmonic vibrational frequencies, infrared and Raman spectra, electronic density, orbital density, ionization potential, electron affinity, joint density of states, optical absorption spectra, site specific polarizabilities, spin Hamiltonians etc. can be calculated. NRLMOL is based on the Kohn-Sham (Schrödinger equation of a system of noninteracting particles generating the same potential as any system of interacting particles) formulation of DFT and solves the Kohn-Sham equations by expressing the Kohn-Sham wave functions as a linear combination of the Gaussian orbitals. The default basis set of the code is particularly optimized for the Perdew-Burke-Ernzerhof (PBE) exchange-correlation energy functional within the Generalized Gradient Approximation (GGA). All the calculations are done at the all electron level and all the systems have a closed shell electronic configuration.

All the contracted basis functions for a given atom are derived from the same set of primitive Gaussians. The number of primitive Gaussians, s-type, p-type and d-type functions as well as the range of the exponents for each kind of atom used in this work, is presented in Table I. This basis set resulted in total 5231($Sc_3N@C_{80}$_ZnTPP), 5261($Y_3N@C_{80}$_ZnTPP), 4723($Sc_3N@C_{80}$_ZnPc) basis functions for the studied systems.

Table I. The numbers of s-, p-, d-type contracted functions, number of primitive gaussians and the range of the gaussian exponents used for each atom.

Atom	s-type	p-type	d-type	Primitives	Exponent range
C	5	4	3	12	$2.22 * 10^4$- 0.077
H	4	3	1	6	7.78 * 10 - 0.074
N	5	4	3	13	$5.17 * 10^4$- 0.094
Sc	7	5	4	19	$156.52 * 10^4$- 0.035
Y	8	6	5	23	$104.62 * 10^5$ - 0.032
Zn	7	5	4	20	$500.8 * 10^4$ - 0.055

The first step in performing the calculations is to optimize the geometry of the systems under study. Geometry optimization means rearranging the position of atoms with respect to each other so that the total force on each individual atom tends to zero. An optimized system is in its minimum energy state.

The ionization potential (IP) of a neutral molecule (with N electrons) is given by the following expression:

$$IP= E(N-1) - E(N)$$

where E(N) is the total energy of the molecule in its ground state and E(N-1) is the total energy of the optimized cation.

Likewise, the electron affinity (EA) of a neutral molecule (with N electrons) is calculated by the following expression:

$$EA=E(N) - E(N+1)$$

where E(N+1) is the total energy of the optimized anion. These are usually called adiabatic IPs and EAs. However, if the structures of the cations and anions are not relaxed (optimized), the calculated energy difference between the optimized neutral structure and the unoptimized ions are called vertical IPs and EAs (14).

Spin-polarized wave functions (Kohn-Sham orbitals) are used for both ground state and excited state calculations. As mentioned earlier, the perturbative delta-SCF method used here to obtain CT excitation energies has already been applied to some other systems such as a set of TCNE-hydrocarbon based D-A complexes and has proved its accuracy and good agreement with experimental results. This method is explicated in references 13 and 16.

According to experimental observations, the dominant photoexcitations of conjugated polymers produce intra-chain singlet excitons (in which the hole and the electron have opposite spins) (6). The electronic excitations that result in electron transfer from the HOMO that typically resides on the donor component to the LUMO which is usually localized on the acceptor are of primary interest in the present study as such excitations impact the open circuit voltage. To get the excitation energy, for instance, for the HOMO to LUMO transition, an electron is removed from the HOMO level and placed in the LUMO orbital, and the self-consistent problem is then solved using the delta-SCF method mentioned above. However, E_M and E_T, the excitation energies of the mixed (a 50-50 blend of pure singlet and triplet states) and triplet states, respectively, need to be calculated in order to get singlet state excitation energies using Ziegler-Rauk method (17,32) .This method determines E_S as $E_S=2E_M-E_T$. The mixed state energy is obtained if the two unpaired electrons in the HOMO and LUMO levels have opposite spins whereas the triplet state energy is obtained if they have the same spins (17).

Chapter 4: Isolated acceptors and donors

The acceptor and donor molecules utilized in this work are: $Sc_3N@C_{80}$, $Y_3N@C_{80}$, ZnTPP (Zinc TetraPhenyl Porphyrin) and ZnPc (Zinc Phthalocyanine). In this chapter the result of calculations performed on these components will be presented.

4.1 $Sc_3N@C_{80}$ AND $Y_3N@C_{80}$ MOLECULES

$Sc_3N@C_{80}$ and $Y_3N@C_{80}$, depicted in figure 9, have the same number of atoms (84 atoms) but different number of electrons (550 and 604, respectively). The structure of $Y_3N@C_{80}$ is not as symmetric as $Sc_3N@C_{80}$'s as verified by Raman and infrared spectroscopy study of these two molecules (24). The average radius of the cage is about 4.11/4.13 Å in Sc_3N/Y_3N trapped systems, respectively. It seems that the cage in $Y_3N@C_{80}$ has expanded in order to accommodate the Y_3N unit. The Sc-N bonds are 2.04 Å and Y-N bonds are 2.06 Å. The average 6-6 C-C bond distances is 1.43/1.45 Å for the $Sc_3N@C_{80}$ and $Y_3N@C_{80}$ systems, respectively while the average 5-6 C-C bonds in both structures is almost the same (1.45 Å). These molecules are employed as the acceptor species. Herein, a few properties of the $Sc_3N@C_{80}$ molecule are described and afterwards the result of the completed calculations of these two systems are presented and compared together.

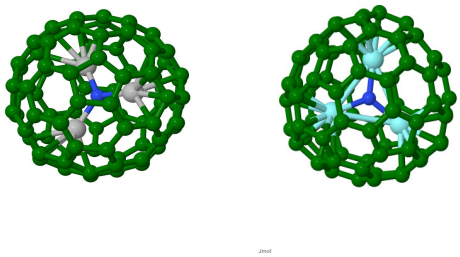

Figure 9. The pictures of $Sc_3N@C_{80}$ and $Y_3N@C_{80}$ molecules in the left and right side, respectively.

$Sc_3N@C_{80}$ is the third most abundant fullerene (after C_{60} and C_{70}) which can be synthesized under normal conditions to date (25). The spherically symmetric C_{80} cage and the endohedral unit Sc_3N do not exist in isolation; however, a stable molecule is formed when they combine together (29). There is evidence that the Sc_3N unit may freely move inside the cage (23). Scandium is the most frequently used metal in construction of trimetallic nitride endohedral fullerenes. The incarceration of Sc_3N cluster is a strongly exothermic mechanism (21). The Sc_3N unit has also been trapped in C_{68} and C_{78} (34). The cage is composed of 12 pentagons and 30 hexagons.

Two isomers have been identified for the $Sc_3N@C_{80}$, one in which the C_{80} cage has an icosahedral (I_h) symmetry and one in which the C_{80} cage possesses a D_{5h} symmetry as illustrated in figure 10. I_h symmetry possessing structures are more abundant. Experimental studies display a trigonal planar geometry for the entrapped Sc_3N cluster in both isomers (34). The I_h-C_{80} cage of $Sc_3N@C_{80}$ is expected to show unique chemical behavior since it possesses pyrene-type sites (a 6-6 bond abutted by a hexagon and a pentagon) and corannulene-type sites (a 6-5 bond abutted by two hexagons), While it does not contain the reactive pyracylene sites (a 6-6 bond abutted by two pentagons) (35). The experimentally measured optical gap energies of ~1.7 eV and ~1.6 eV have been reported for the $Sc_3N@I_h$-C_{80} and $Sc_3N@D_{5h}$-C_{80} systems, respectively. Therefore, both isomers of this molecule are categorized as large band gap fullerenes, considering 1 eV band gap as the boundary of large band gap and low band gap fullerenes (34).

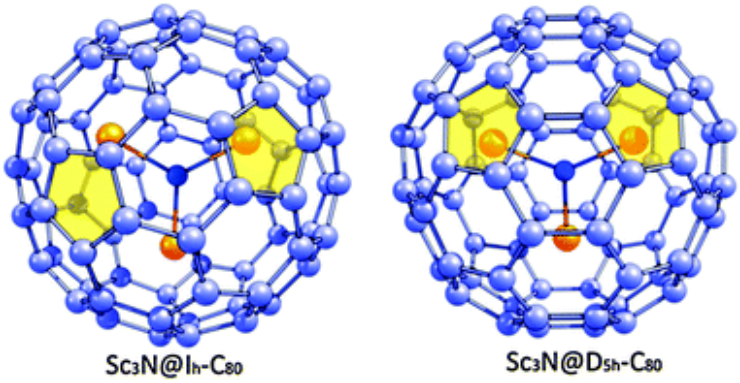

Figure 10. The two isomers of $Sc_3N@C_{80}$ molecule.

The evaluation of the electronic properties of this molecule suggests a transfer of six electrons from the endohedral unit Sc_3N to the cage, making it a negatively charged surface and giving rise to $[Sc_3N]^{+6}@[C_{80}]^{-6}$ (24,34), causing a closed shell configuration for the endohedral fullerene (23).

In general, fullerenes show large electron affinities (due to having low-lying unoccupied orbitals (23)), large charge accumulation capacity along with low reorganization energies in CT reactions that make them good candidates as acceptors in D-A complexes (17,20,36-38).

$Sc_3N@C_{80}$ like C_{60} possesses small reorganization energies during charge transfer reactions (22). Its utilization as the acceptor component in OPVs improves the lifetime of the charge-separated state and puts it in the order of microseconds (while these lifetimes are typically in the order of nanoseconds (28)) (22).

Figures 11 and 12, illustrate the ground state density of states (DOS) of the $Sc_3N@C_{80}$ and $Y_3N@C_{80}$ molecules, projected on their corresponding components. In these figures the red line

indicates the Fermi energy level. Therefore, the states on the left side of the red line are the occupied states and the states on its right side are the unoccupied ones.

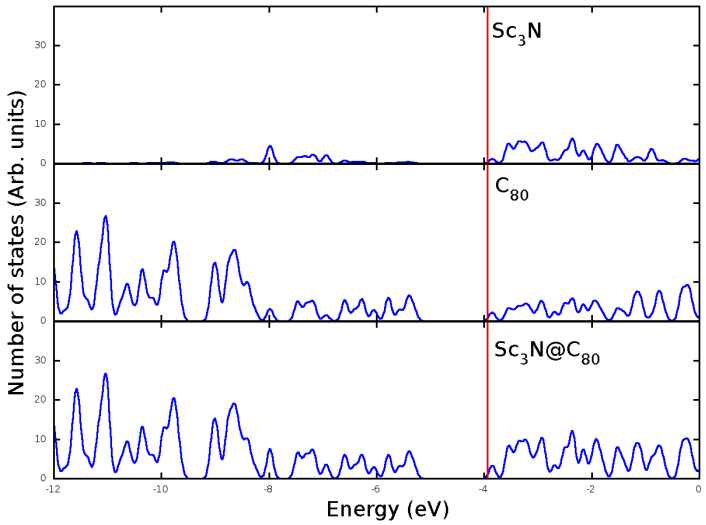

Figure 11. The total ground state density of states of the $Sc_3N@C_{80}$ fullerene, projected on its components.

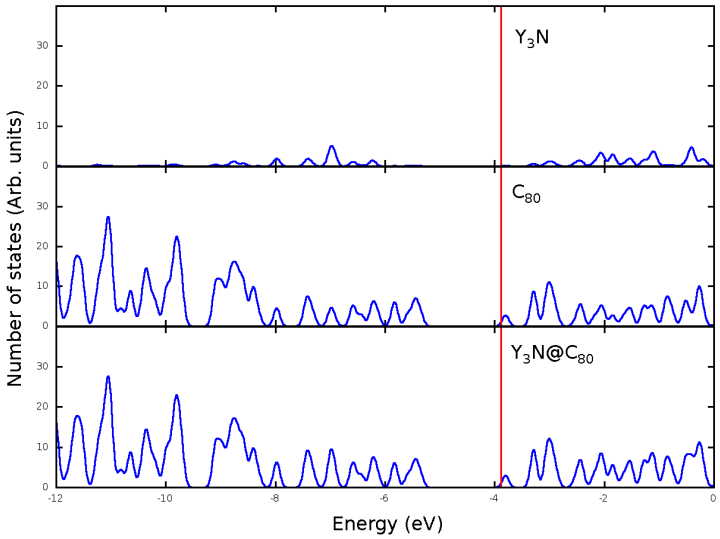

Figure 12. The total ground state density of states of $Y_3N@C_{80}$ fullerene, projected on its components.

As the plots demonstrate, in the two molecules the HOMO orbital is localized on the C_{80} cage. In $Sc_3N@C_{80}$, both the endohedral unit Sc_3N and C_{80} cage contribute to the construction of the LUMO level of the molecule while in $Y_3N@C_{80}$, the LUMO orbital is entirely localized on the C_{80} cage. Furthermore, the Sc_3N cluster has a larger number of low-lying unoccupied states compared with its counterpart Y_3N unit. The energy levels of the C_{80} cage do not show significant changes when altering the trapped unit inside it from Sc_3N to Y_3N. The orbital densities of six low-lying orbitals of these structures, spanning the hole orbitals from HOMO to HOMO-2 and particle orbitals from LUMO to LUMO+2, also verify the above statements. However, these pictures are static and investigating the above facts needs direct use of the visualization software that allows the rotation of the structures. These plots are displayed in figures 13 and 14.

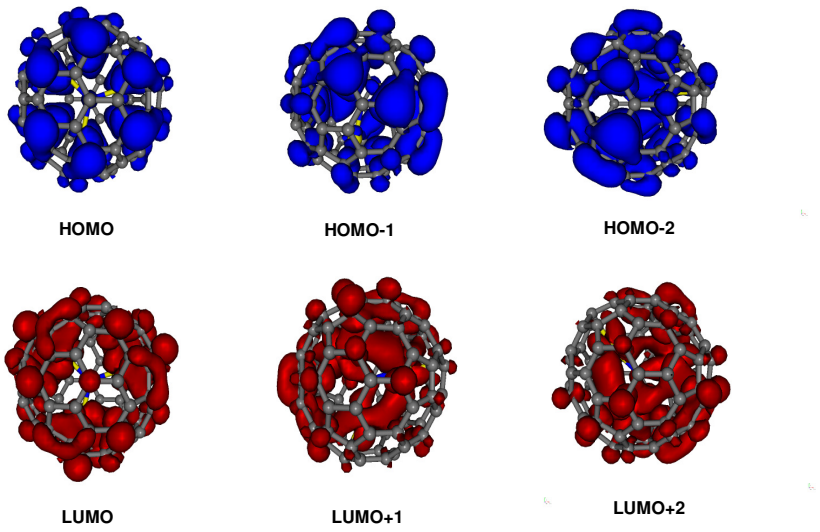

Figure 13. The electron densities of the HOMO (blue) and the LUMO (red) orbitals of $Sc_3N@C_{80}$ fullerene.

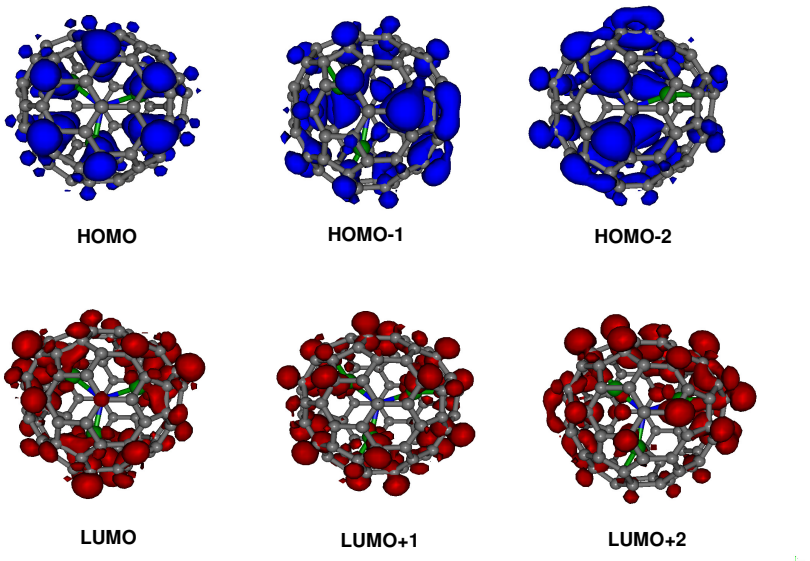

Figure 14. The electron densities of the HOMO (blue) and the LUMO (red) orbitals of $Y_3N@C_{80}$ fullerene.

The DFT calculated adiabatic/vertical ionization potential, adiabatic/vertical electron affinity, quasiparticle gap, exciton binding energy, ground state HOMO-LUMO gap and HOMO-LUMO excitation energy of the $Sc_3N@C_{80}$ and $Y_3N@C_{80}$ are tabulated in Table II.

Table II. The DFT calculated IP, EA, quasiparticle gap, exciton binding energy, ground state H-L gap and H-L excitation energy of $Sc_3N@C_{80}$ and $Y_3N@C_{80}$ fullerenes.

system	**IP/vIP (eV)**	**EA/vEA (eV)**	**quasiparticle gap (eV)**	**exciton binding energy (eV)**	**gs_HOMO-LUMO gap/ HOMO-LUMO E_{ex} (eV)**
$Sc_3N@C_{80}$	6.65/6.68	2.28/2.25	4.37	2.85	1.48/1.52
$Y_3N@C_{80}$	6.69/6.73	2.49/2.46	4.2	2.59	1.55/1.61

The HOMO-LUMO gap as obtained from the Kohn-Sham eigenvalues does not present the correct corresponding excitation energies for two reasons. Firstly, because DFT

underestimates the gap due to missing derivative discontinuity and self-interaction correction, secondly since this gap does not consider the particle-hole interaction and passive orbitals' polarization (14).

The quasiparticle (fundamental) gap is given by the following expression:

$$E\ (\text{quasiparticle gap}) = IP - EA$$

And the exciton binding energy is calculated as follows:

$$E\ (\text{exciton binding energy}) = E\ (\text{quasiparticle gap}) - E\ (\text{optical gap})$$

where the optical gap is the same as the HOMO-LUMO excitation energy. The optical band gap determines the portion of the solar irradiation which is absorbed by the molecule. If the exciton binding energy of a material is large, there will be a distinction between the optical band gap and the electrical band gap. The optical band gap is the threshold for the absorption of the photons while the electrical band gap is the threshold of the creation of an unbound electron-hole pair. Thus, in most of the inorganic materials where the exciton binding energies are small, the optical and electrical band gaps are almost identical but there is a noticeable distinction between them in organic materials.

The calculated IP and EA of the $Y_3N@C_{80}$ are larger than $Sc_3N@C_{80}$'s, verifying that the electrochemical behaviors of the trimetallic nitride endohedral fullerenes depend on the nature of the encapsulated cluster. The calculated exciton binding energies suggest that exciton dissociation should be an easier process for the $Y_3N@C_{80}$ compared with that of $Sc_3N@C_{80}$.

The calculated ground state dipole moment of $Sc_3N@C_{80}$ is significantly larger than $Y_3N@C_{80}$'s (0.25 versus 0.025 Debye).

A few excitation energies for the two systems, applying the perturbative delta-SCF method, are given in Table III. The triplet state energies are given in parentheses.

Table III. A few excitation energies for $Sc_3N@C_{80}$ and $Y_3N@C_{80}$ molecules. The energies of the triplet states are given in parentheses. All energies are in eV.

Transition	**$Sc_3N@C_{80}$ Singlet (triplet) State E_{ex} (eV)**	**$Y_3N@C_{80}$ Singlet (triplet) State E_{ex} (eV)**
HOMO → LUMO	**1.52**(1.47)	**1.61**(1.56)
HOMO → LUMO+1	1.89(1.86)	2.13(2.04)
HOMO → LUMO+2	1.9(1.87)	2.15(2.1)
HOMO → LUMO+3	1.95(1.88)	2.15(2.1)
HOMO → LUMO+4	2.17(2.13)	2.38(2.32)
HOMO → LUMO+5	2.13(2.08)	2.38(2.32)
HOMO-1 → LUMO	1.62(1.56)	1.7(1.65)
HOMO-1 → LUMO+1	2.09(2.05)	2.2(2.14)
HOMO-1 → LUMO+2	2.11(2.06)	2.25(2.17)
HOMO-1 → LUMO+3	2.02(1.99)	2.25(2.18)
HOMO-1 → LUMO+4	**2.48**(2.44)	**2.47**(2.41)
HOMO-1 → LUMO+5	2.38(2.33)	**2.47**(2.4)
HOMO-2 → LUMO	1.63(1.57)	1.7(1.65)
HOMO-2 → LUMO+1	2.13(2.08)	2.2(2.14)
HOMO-2 → LUMO+2	2.13(2.09)	2.25(2.18)
HOMO-2 → LUMO+3	2.02(1.98)	2.25(2.17)
HOMO-2 → LUMO+4	2.41(2.37)	2.46(2.4)
HOMO-2 → LUMO+5	2.38(2.35)	**2.47**(2.41)

As tabulated, the excitation energies lie within a range of 1.52 eV-2.48 eV for the $Sc_3N@C_{80}$ and 1.61eV-2.47 eV for the $Y_3N@C_{80}$ molecule. Furthermore, the allowed and forbidden transitions are checked and the results are displayed in Table IV.

Table IV. The square of the dipole moment magnitude for a few transitions of the $Sc_3N@C_{80}$ and $Y_3N@C_{80}$ fullerenes. This values show if these transitions are light or dark.

Transition	$Sc_3N@C_{80}$ $(\text{dipole moment})^2$	$Y_3N@C_{80}$ $(\text{dipole moment})^2$
HOMO → LUMO	0.739338	0.940436
HOMO → LUMO+1	0.750729	**4.25068**
HOMO → LUMO+2	0.754615	3.491843
HOMO → LUMO+3	**2.915238**	3.503316
HOMO → LUMO+4	1.223876	0.777228
HOMO → LUMO+5	1.219279	0.776201
HOMO-1 → LUMO	0.424439	0.788694
HOMO-1 → LUMO+1	1.641042	**4.024486**
HOMO-1 → LUMO+2	0.372764	3.168432 or 1.928556
HOMO-1 → LUMO+3	1.386317	3.168432 or 1.928556
HOMO-1 → LUMO+4	1.117169	0.178489 or 0.457747
HOMO-1 → LUMO+5	0.982163	0.178489 or 0.457747
HOMO-2 → LUMO	0.423246	0.788888
HOMO-2 → LUMO+1	0.375047	**4.053734**
HOMO-2 → LUMO+2	1.649137	1.916340 or 3.170770
HOMO-2 → LUMO+3	1.391922	1.916340 or 3.170770
HOMO-2 → LUMO+4	0.974679	0.473157 or 0.170580
HOMO-2 → LUMO+5	1.122537	0.473157 or 0.170580

As it can be derived from the table, all the indicated transitions are optically allowed (or so-called bright), although with different probabilities. The probability of the occurrence of HOMO to LUMO+3 transition for the $Sc_3N@C_{80}$ shows to be the highest. On the other hand, for the $Y_3N@C_{80}$ molecule, the incidence of HOMO, HOMO-1, as well as HOMO-2 to LUMO+1 transitions, are the most probable ones. In addition, it is learned that HOMO-1 and HOMO-2, LUMO+1 and LUMO+2, as well as LUMO+4 and LUMO+5 orbitals, are the degenerate states of the $Sc_3N@C_{80}$ molecule. On the other hand, HOMO-1 and HOMO-2, LUMO+2 and LUMO+3, as well as LUMO+4 and LUMO+5 orbitals, are the degenerate states of the

$Y_3N@C_{80}$. The reason of reporting two values for some of the transitions in the table is the degeneracy of the corresponding orbitals.

4.2 ZnTPP (Zinc TetraPhenyl Porphyrin) and ZnPc (Zinc Phthalocyanine) molecules

In the early 1960s, the semiconducting properties of dyes were discovered and they were one of the first organic materials to display photovoltaic effect (9). Furthermore, in order to harvest a large amount of solar energy, materials that are employed as the light absorber ought to have high absorption coefficients in the region with wavelengths below 700 nm, since almost half of the solar irradiation lies in this region. This is a region greatly covered with porphyrin and phthalocyanine derivatives. The utilization of porphyrins and phthalocyanines as donor moieties has had a great role in understanding and improvement of the OPVs (28).

ZnTPP ($ZnC_{44}H_{28}N_4$) is composed of 77 atoms and 350 electrons. Its structure is illustrated in figure 15. The use of porphyrins and metalloporphyrins as donors is triggered by the natural light harvesting systems. They act as chromophores. In ZnTPP, a phenyl group is added to each of the four carbon meso-positions of the zinc-porphyrin molecule (20). The molecular structures, optical spectra and electronic properties of porphyrins and their derivatives are versatile and variable, making them basic materials in OPV devices (28).

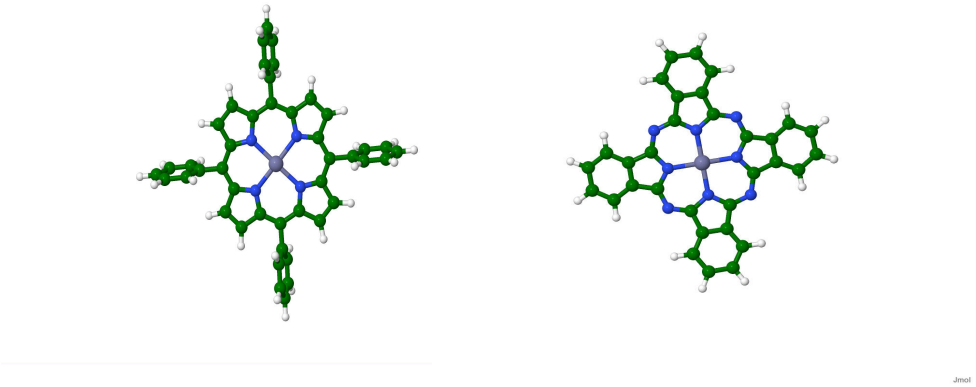

Figure 15. The pictures of ZnTPP and ZnPc molecules in the left and right side, respectively.

On the other hand, ZnPc ($ZnC_{32}H_{16}N_8$) has 57 atoms and 294 electrons. It is depicted in figure 15. Phthalocyanine (Pc) ($C_{32}H_{18}N_8$), a p-type semiconductor, is a blue-green-colored compound (2), illustrated in figure 16.

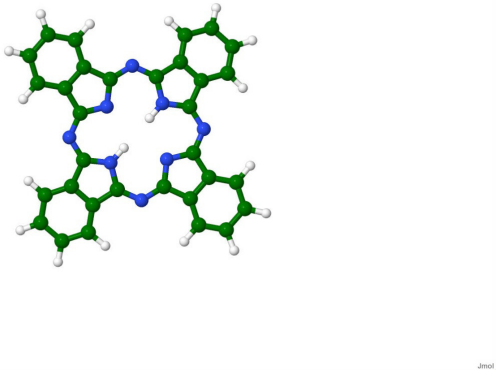

Figure 16. The picture of Phthalocyanine molecule.

Thin films of phthalocyanine with thicknesses of only a few tens-of –nm absorb about 50-70% of the incident visible light. Furthermore, phthalocyanine demonstrates stability under illumination both in air and in a wet environment. On the other hand, in order to enhance short-circuit current densities which is one of the factors leading to larger PCEs, it is necessary to have a high exciton mobility and rigid planar structures like Pc to favor this feature (1). Phthalocyanines also show very high exciton diffusion lengths due to their highly planar structures (28).

The DFT obtained adiabatic/vertical ionization potential, adiabatic/vertical electron affinity, quasiparticle gap, exciton binding energy, ground state HOMO-LUMO gap and HOMO-LUMO excitation energy of ZnTPP and ZnPc are tabulated in Table V.

Table V. The DFT calculated IP, EA, quasiparticle gap, exciton binding energy, ground state H-L gap and H-L excitation energy of ZnTPP and ZnPc molecules.

system	**IP/vIP (eV)**	**EA/vEA (eV)**	**quasiparticle gap (eV)**	**exciton binding energy (eV)**	**gs_HOMO-LUMO gap/ HOMO-LUMO E_{ex} (eV)**
ZnTPP	6.29/6.32	1.23/1.22	5.06	2.97	1.91/2.09
ZnPc	6.34/6.36	1.76/1.72	4.58	3.02	1.4/1.56

Furthermore, the ground state dipole moments turn out to be 0.12 and 0.19 Debye, for the ZnTPP and ZnPc molecules, respectively.

Figures 17 and 18, display the ground state density of states of the two molecules. The highest two occupied and lowest two unoccupied orbitals of porphyrin are known as Gouterman orbitals which characterize the absorption bands of porphyrin in isolation (20,33).

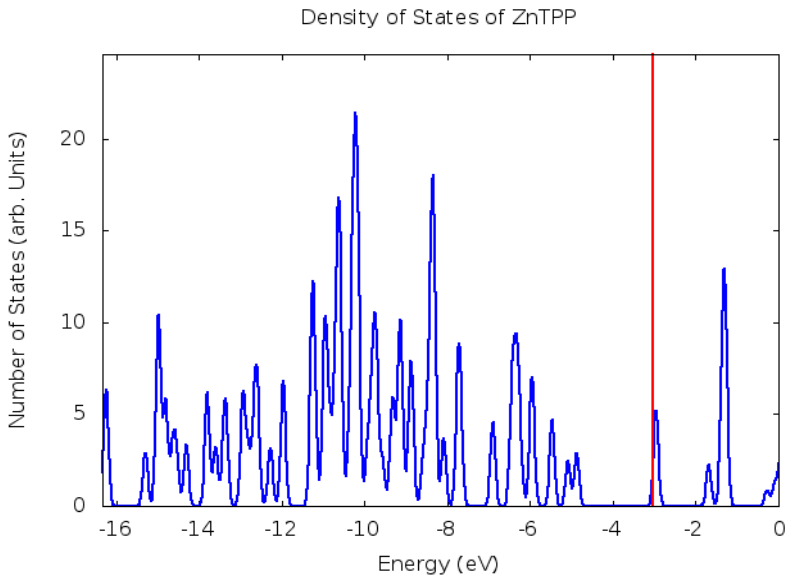

Figure 17. The ground state density of states of Zinc TetraPhenyl Porphyrin molecule.

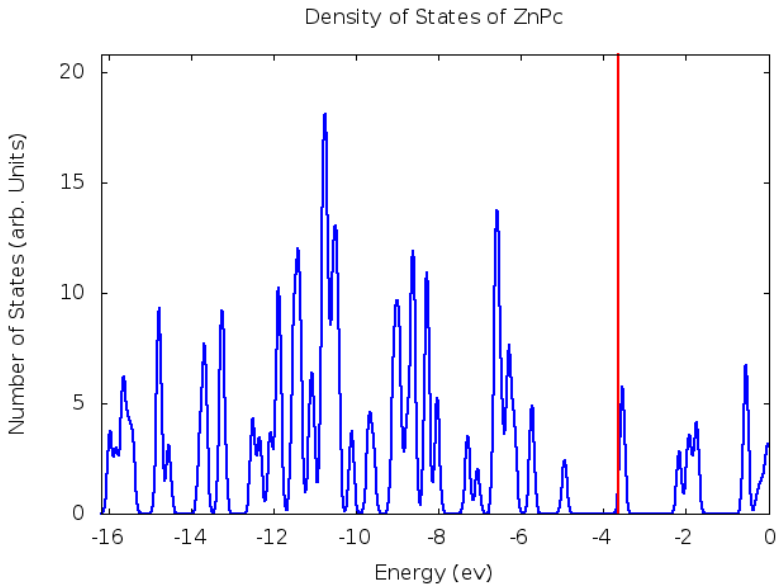

Figure 18. The ground state density of states of Zinc Phthalocyanine molecule.

Figures 19 and 20, depict orbital density of a few low-lying orbitals of these two molecules.

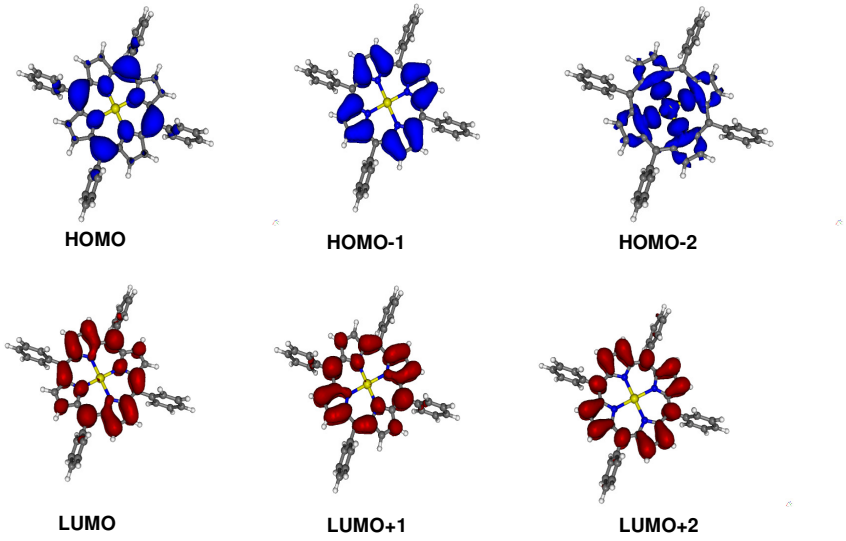

Figure 19. The electron densities of the HOMO (blue) and the LUMO (red) orbitals of ZnTPP.

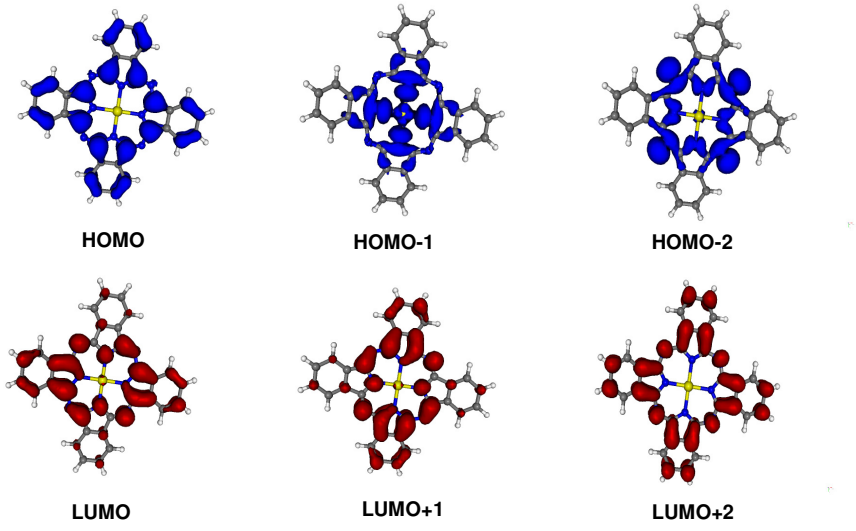

Figure 20. The electron densities of the HOMO (blue) and the LUMO (red) orbitals of ZnPc.

Table VI, shows excited state energies of ZnTPP and ZnPc donors for a few low-lying transitions. Both singlet and triplet excitation energies are reported. .

Table VI. A few excitation energies for ZnTPP and ZnPc molecules. The energies of the triplet states are given in parentheses. All energies are in eV.

Transition	**ZnTPP Singlet (triplet) State E_{ex} (eV)**	**ZnPc Singlet (triplet) State E_{ex} (eV)**
HOMO → LUMO	**2.09**(1.78)	**1.56**(1.34)
HOMO → LUMO+1	**2.09**(1.78)	1.58(1.34)
HOMO → LUMO+2	3.38(3.11)	2.88(2.76)
HOMO → LUMO+3	3.88(3.88)	3.14(2.98)
HOMO → LUMO+4	4.02(4.01)	3.23(3.09)
HOMO → LUMO+5	4.04(4.02)	3.29(3.41)
HOMO-1 → LUMO	2.23(2.03)	2.76(2.76)
HOMO-1 → LUMO+1	2.23(2.03)	2.69(2.68)
HOMO-1 → LUMO+2	3.49(3.33)	4.11(4.1)
HOMO-1 → LUMO+3	4.14(4.13)	4.34(4.28)
HOMO-1 → LUMO+4	4.27(4.25)	(4.41)
HOMO-1 → LUMO+5	4.27(4.24)	4.74(4.66)
HOMO-2 → LUMO	2.97(2.93)	2.87(2.86)
HOMO-2 → LUMO+1	2.97(2.93)	3.27(2.8)
HOMO-2 → LUMO+2	4.31(4.30)	4.42(4.34)
HOMO-2 → LUMO+3	5.1(5.1)	4.54(4.52)
HOMO-2 → LUMO+4	5.24(5.23)	4.68(4.66)
HOMO-2 → LUMO+5	**5.26**(5.26)	**4.81**(4.88)

As it can be seen from the table, the calculated excited state energies lie within a range of 2.09 eV-5.26 eV for the ZnTPP molecule and 1.56 eV-4.81 eV for the ZnPc structure. Moreover, in order to find out which of these transitions are optically allowed, more studies were conducted. The results of these calculations are shown in Table VII. The table indicates that the HOMO to LUMO and LUMO+1, as well as HOMO-1 to LUMO and LUMO+1 transitions are

the most probable ones for the ZnTPP while the transitions marked with an asterisk are expected to occur rarely. Furthermore, LUMO and LUMO+1, as well as LUMO+4 and LUMO+5 orbitals are found to be the degenerate states of this molecule.

Table VII. The square of the dipole moment magnitude for a few transitions of the ZnTPP and ZnPc molecules. This values show if these transitions are light or dark.

Transition	**ZnTPP** **(dipole moment)^2**	**ZnPc** **(dipole moment)^2**
HOMO → LUMO	**9.815002**	**17.170106**
HOMO → LUMO+1	**9.642408**	**17.187244**
HOMO → LUMO+2	0.000195*	0.104546
HOMO → LUMO+3	0.162595	0.000844*
HOMO → LUMO+4	0.000796*	0.000174*
HOMO → LUMO+5	0.000105*	0.044504
HOMO-1 → LUMO	**10.984235**	0.068643
HOMO-1 → LUMO+1	**10.925894**	0.060694
HOMO-1 → LUMO+2	0.000437*	0.000981*
HOMO-1 → LUMO+3	0.03941	0.009038
HOMO-1 → LUMO+4	0.000101*	0.000847*
HOMO-1 → LUMO+5	0.000557*	0.012149
HOMO-2 → LUMO	0.005047	0.076467
HOMO-2 → LUMO+1	0.005417	0.094511
HOMO-2 → LUMO+2	0.003017	0.054402
HOMO-2 → LUMO+3	0.000022*	0.000053*
HOMO-2 → LUMO+4	0.018421	0.000011*
HOMO-2 → LUMO+5	0.016395	0.000431*

On the other hand, HOMO to LUMO and LUMO+1 transitions form the most probable bright transitions of the ZnPc compound. The transitions indicated with an asterisk in the table, have the weakest possibility of occurrence. Finally, LUMO and LUMO+1orbitals are two degenerate states of this molecule.

Chapter 5: Effect of different orientations of fullerene cage's endohedral unit on electronic properties of $Sc_3N@C_{80}$_ZnTPP dyad

Porphyrin-Fullerene (PF) pairs are one of the most widely studied organic donor-acceptor constructs (20,39,40). In most of the PF dyads, the fullerene is attached to the porphyrin through different linker molecules and the center-to-center distance ranges from 6.5 to 7 Å (20,40,41). $Sc_3N@C_{80}$_ZnTPP molecule, a PF conjugate, is made up of 161 atoms and 900 electrons. In this complex, $Sc_3N@C_{80}$ plays the role of the acceptor component and ZnTPP (Zinc TetraPhenyl Porphyrin) is the donor part. In this chapter, two isomers of this dyad, called $Sc_3N@C_{80}$_ZnTPP (5-6) and $Sc_3N@C_{80}$_ZnTPP (6-6) are analyzed. These two isomers are depicted in figure 21. These are non-bonded structures with a face-to-face distance of about 3.2 Å. However, only a few experimental studies have been performed on non-bonded PF pairs. Most of them have investigated covalently linked systems (20).

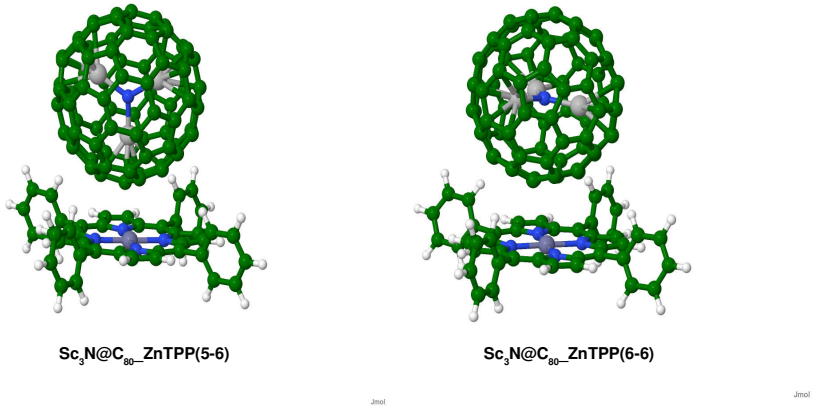

Figure 21. The pictures of the two isomers of $Sc_3N@C_{80}$_ZnTPP dyad, called 5-6 and 6-6. They are different in the orientation of the endohedral unit inside the cage.

As pictures display, these molecules are studied in co-facial geometry. Different orientations of the endohedral unit inside the cage make the two structures distinct. In the so-called 5-6 dyad, the endohedral moiety, which forms a planar molecule, is perpendicularly positioned with respect to the ZnTPP plane. However, in the 6-6 complex, this unit is parallel to the porphyrin's plane. The purpose of this chapter is to study the effect of this different orientation on the ground and excited state electronic structure of this D-A pair.

The DFT calculated adiabatic/vertical ionization potential, adiabatic/vertical electron affinity, quasiparticle gap, exciton binding energy, ground state HOMO-LUMO gap and HOMO-LUMO excitation energy of both systems are tabulated in Table VIII.

Table VIII. . The DFT calculated IP, EA, quasiparticle gap, exciton binding energy, ground state H-L gap and H-L excitation energy of the two isomers of $Sc_3N@C_{80}$_ZnTPP dyad, called 5-6 and 6-6.

	IP/vIP (eV)	**EA/vEA (eV)**	**quasiparticle gap (eV)**	**exciton binding energy (eV)**	**gs_HOMO-LUMO gap/ HOMO-LUMO E_{ex} (eV)**
(5-6)	6.12/6.13	----/2.50	3.63	1.47	1.167/2.16
(6-6)	----/6.08	2.25/2.23	3.85	1.74	1.054/2.11

The quasi particle gap given by IP-EA which determines the charge transfer excitation energy at infinite separation is 0.22 eV larger in the 6-6 complex. However, exciton binding energy for this dyad has a higher value, turning the exciton splitting more difficult and suggesting a greater overlap for the particle and hole orbitals of this molecule. Ground state HOMO-LUMO gaps do not show any significant difference. Furthermore, the total energies (not given here) of these two macromolecules differ by only about 29 meV.

Table IX, provides useful information in order to study how the energy levels shift upon complex formation. It shows DFT calculated ionization potential of the donor and electron affinity of the acceptor in isolation and in complexes. For the 6-6 dyad, the vertical ionization potential and vertical electron affinity are given.

Table IX. The DFT calculated ionization potential (IP) of the donor and electron affinity (EA) of the acceptor in isolation and in complexes.

System	**$Sc_3N@C_{80}$**	**ZnTPP**	**$Sc_3N@C_{80}$_ZnTPP (5-6)**	**$Sc_3N@C_{80}$_ZnTPP (6-6)**
IP (eV)		6.29	6.12	6.08 (vIP)
EA (eV)	2.28		2.50(vEA)	2.23(vEA)

The results show that the Zn-porphyrin HOMO is shifted in the same direction, in both isomers and it is raised by 0.17 eV and 0.21 eV in 5-6 and 6-6 complexes, respectively. On the other hand, the fullerene LUMO is lowered by 0.22 eV in 5-6 isomer but raised by 0.05 eV in 6-6 dyad. The upward shift of Zn-porphyrin HOMO is almost the same in both complexes; however, the upward shift of the fullerene LUMO upon complexation in 6-6 construct along with the fact of its downward shift in the 5-6 complex makes us to anticipate a higher value of open circuit voltage for the 6-6 isomer of the $Sc_3N@C_{80}$_ZnTPP molecule.

The ground state density of states (DOS) of the 5-6 and 6-6 isomers, projected on their corresponding donor and acceptor components, are illustrated in figures 22 and 23. They are almost identical. In these graphs, the red line denotes the Fermi level. Therefore, the states on the left side of the red line represent the occupied states while the states on the right side of the red line exhibit the unoccupied states. From these plots, the contribution of the donor and acceptor

molecules' orbitals in constructing the HOMO and LUMO level of the complex can be discovered.

Likewise, the results of the fragment analysis demonstrate the contribution of the orbitals of the donor and acceptor molecules in the construction of the orbitals of the complex. This analysis was performed on the 5-6 dyad, revealing that the HOMO and HOMO-1 orbitals of this complex are the porphyrin occupied Gouterman orbitals and LUMO and LUMO+1 orbitals of the $Sc_3N@C_{80}$ form the LUMO and LUMO+1 orbitals of the complex.

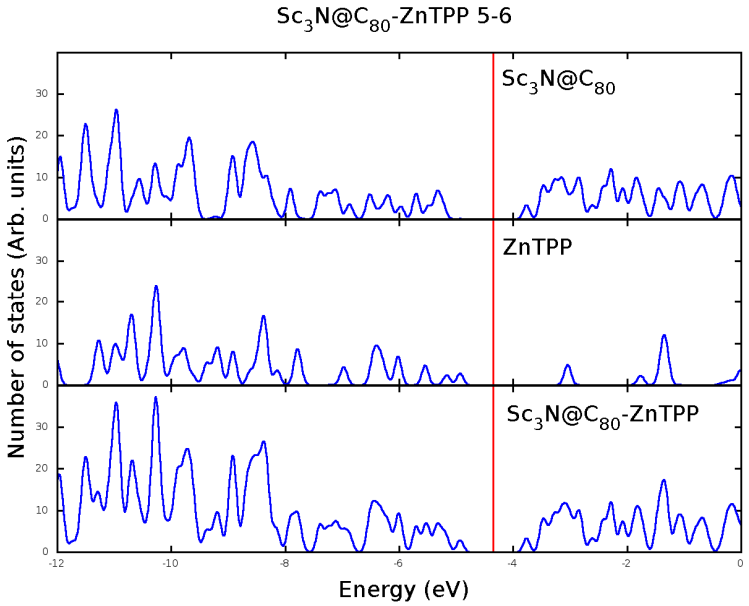

Figure 22. The total ground state density of states of $Sc_3N@C_{80}$_ZnTPP (5-6) dyad, projected on its components.

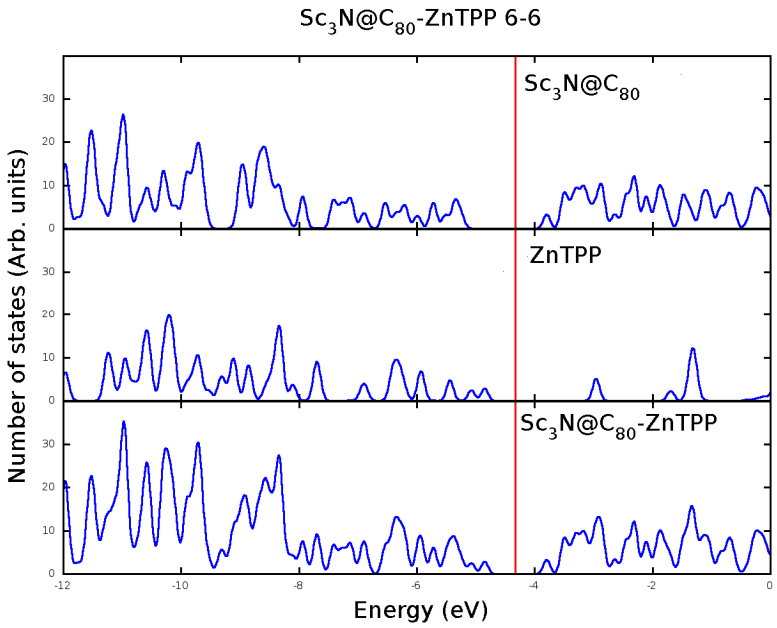

Figure 23. The total ground state density of states of $Sc_3N@C_{80}$_ZnTPP (6-6) dyad, projected on its components.

In both cases the HOMO orbital is localized on the Zn-porphyrin fragment and the LUMO sits on the fullerene component. Therefore, the HOMO to LUMO transition is a charge transfer transition. In addition, the two of them have several low-lying closely spaced unoccupied orbitals above the LUMO level, a property attributed to the employment of trimetallic nitride endohedral fullerene $Sc_3N@C_{80}$ molecule, as the acceptor component.

Figures 24 and 25, show a few low-lying CT excited state transitions from the porphyrin Gouterman orbitals to the $Sc_3N@C_{80}$ LUMOs, by arrows originating from the ZnTPP donor states displayed on the left side to the corresponding $Sc_3N@C_{80}$ acceptor states depicted on the right side.

The plots verify that HOMO and HOMO-1 orbitals of the both complexes are localized on the donor, ZnTPP moiety and the LUMO, LUMO+1 and LUMO+2 orbitals are localized on the acceptor, $Sc_3N@C_{80}$ molecule. Thus, since these orbitals sit on their respective donor/acceptor component, the transitions correspond to CT excited states. However, for the both complexes, the HOMO-2 orbital (not shown) is localized on the fullerene. Therefore, none of the HOMO-2 to LUMO, LUMO+1 or LUMO+2 transitions constitutes a CT state. These transitions are named local excitations.

The lowest DFT calculated CT excitation energies for the 5-6 and 6-6 pairs are 2.16 eV and 2.11 eV, respectively.

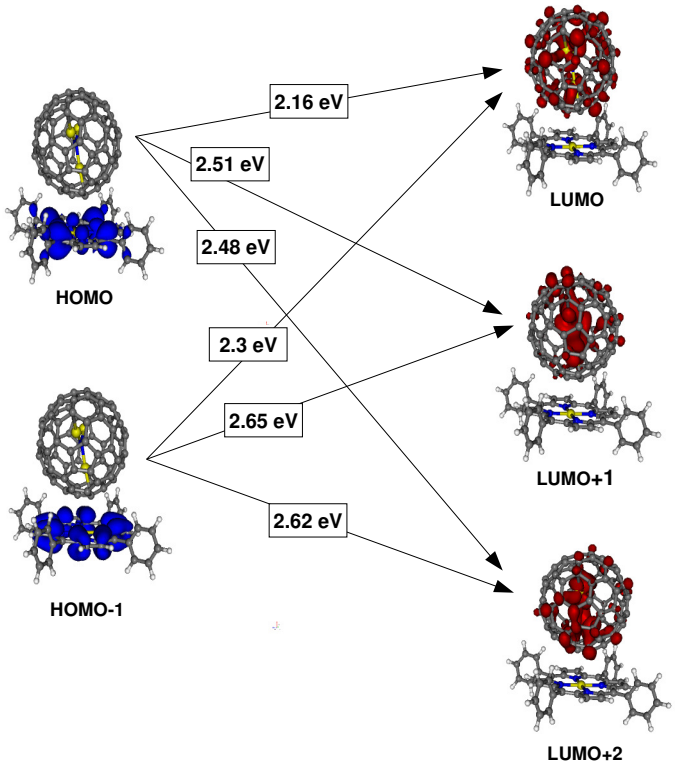

Figure 24. The lowest few charge transfer excitation energies in $Sc_3N@C_{80}$_ZnTPP (5-6).

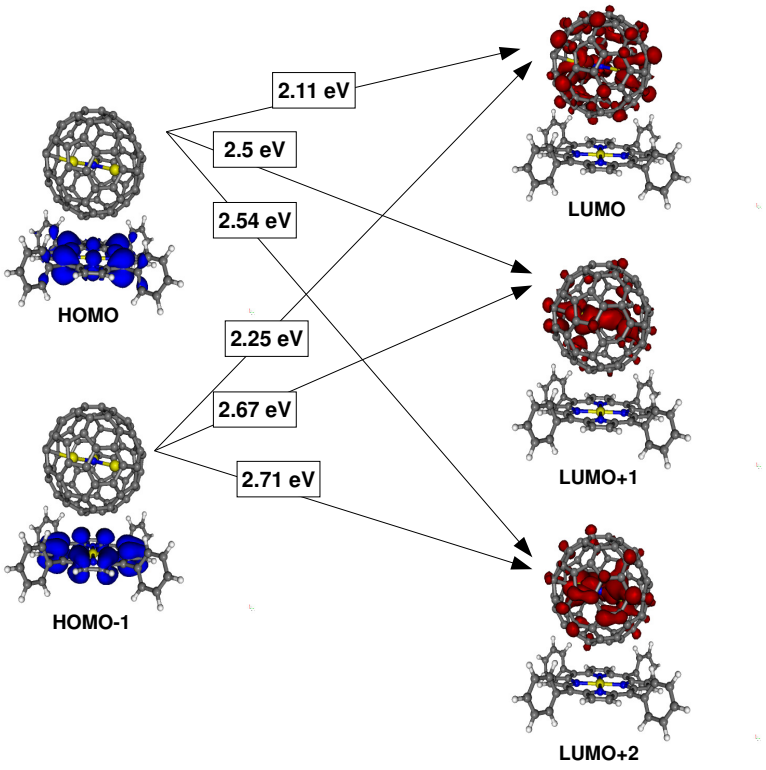

Figure 25. The lowest few charge transfer excitation energies in $Sc_3N@C_{80}$_ZnTPP (6-6).

The energies of the excited states of the two systems are tabulated in Table X. In the table, transitions that are corresponding to the local excitations (charge transfer on the same component) are indicated with an asterisk. Both the singlet and triplet excited state energies of the single particle excitations are presented. The singlet excited state energies are calculated using the prescribed Ziegler et al. Formula, as described before. These calculations are done in gas phase, ignoring all solvent effects and the ionic relaxations upon excitation. The experimentally measured CT energies for covalently linked C_{60}_ZnP with a co-facial orientation range from 1.27 to 1.86 eV depending on solvent polarity, topology and linker (20,42-44).

The calculated CT excitation energies range from 2.16 eV/2.11 eV to 3.1 eV/3.1 eV in the 5-6/6-6 complexes. The results are almost the same as the highest difference in the corresponding transitions is only 0.09 eV, occurring for the H-1 to L+2 and H-1 to L+3 transitions where these transitions for the 6-6 isomer show higher values. Comparing these results with previously calculated CT excited state energies for two similar systems, employing the same donors (ZnTPP) but empty fullerenes (C_{60} and C_{70}) as acceptors reveals the advantage of applying the endohedral metallofullerenes as the acceptor component in OPVs. The lowest DFT calculated CT excitation energies, occurring for HOMO to LUMO+1 transition in both, are 1.68 eV/1.95 eV in C_{60}_ZnTPP and C_{70}_ZnTPP dyads, respectively (20).

Table X. A few excitation energies for the $Sc_3N@C_{80}$_ZnTPP isomers, called 5-6 and 6-6. The energies of the triplet states are given in parentheses. All energies are in eV.

Transition	**$Sc_3N@C_{80}$_ZnTPP(5-6) Singlet (triplet) State E_{ex} (eV)**	**$Sc_3N@C_{80}$_ZnTPP(6-6) Singlet (triplet) State E_{ex} (eV)**
HOMO → LUMO	2.16 (2.15)	2.11 (2.1)
HOMO → LUMO+1	2.51 (2.5)	2.5 (2.5)
HOMO → LUMO+2	2.48 (2.47)	2.541 (2.538)
HOMO → LUMO+3	2.46 (2.43)	2.543 (2.537)
HOMO → LUMO+4	2.96 (2.96)	2.91 (2.91)
HOMO → LUMO+5	2.87 (2.86)	2.89 (2.88)
HOMO-1 → LUMO	2.3 (2.28)	2.25 (2.24)
HOMO-1 → LUMO+1	2.65 (2.63)	2.67 (2.66)
HOMO-1 → LUMO+2	2.62 (2.61)	2.71 (2.7)
HOMO-1 → LUMO+3	2.61 (2.58)	2.7 (2.69)
HOMO-1 → LUMO+4	3.1 (3.08)	3.1 (3.1)
HOMO-1 → LUMO+5	3.02 (3.00)	3.07 (3.06)
HOMO-2 → LUMO	1.52 (1.48)*	1.51 (1.47)*
HOMO-2 → LUMO+1	1.87 (1.84)*	1.87 (1.84)*
HOMO-2 → LUMO+2	1.88 (1.85)*	1.9 (1.868)*
HOMO-2 → LUMO+3	1.95 (1.89)*	1.93 (1.874)*
HOMO-2 → LUMO+4	2.19 (2.15)*	2.14 (2.1)*
HOMO-2 → LUMO+5	2.19 (2.15)*	2.12 (2.08)*

The ground state dipole moments of the 5-6 and 6-6 complexes are 0.665 and 0.585 Debye, respectively and the excited triplet(mixed) state dipole moments for the HOMO-LUMO excitations are 21.18(21.21) Debye for the 5-6 and 24.33(24.36) Debye for the 6-6 dyad. However, since in calculation of the charge transfer excitation energies the ionic relaxations are ignored, the dipole moments only indicate the rearrangement in electronic density (20).

It can be concluded that the orientation of the endohedral unit inside the cage hardly affects the ground state electronic structure of this complex. The close values of calculated IPs and EAs for the two isomers as well as the extremely similar ground state density of states for the two, are referred to as supporting evidences for the above statement. This result can be attributed to the reduced interaction between the encapsulated cluster and the porphyrin. Moreover, the obtained CT excitation energies showed negligible differences, suggesting that the two systems will cause almost the same open circuit voltages when applied in OPVs. However, these CT excited state energies showed higher values when compared to the similar systems with C_{60} and C_{70} as acceptors, verifying the direct positive influence of utilizing trimetallic nitride endohedral fullerenes as the acceptor component in D-A conjugates exploited in OPV devices.

Chapter 6: Effect of changing the donor or the acceptor component on electronic properties of $Sc_3N@C_{80}$_ZnTPP complex

Herein, three different non-bonded D-A complexes are studied. They are comprised of Zinc TetraPhenyl Porphyrin (ZnTPP) and Zinc Phthalocyanine (ZnPc) as donors and $Sc_3N@C_{80}$ and $Y_3N@C_{80}$ as acceptors. The purpose is to examine the changes in ground and excited state electronic structure of the $Sc_3N@C_{80}$_ZnTPP dyad as the donor or the acceptor component is changed. The three different donor-acceptor pairs studied are as follows: $Sc_3N@C_{80}$_ZnTPP, $Y_3N@C_{80}$_ZnTPP and $Sc_3N@C_{80}$_ZnPc. They are all studied in co-facial orientation. Since the $Sc_3N@C_{80}$_ZnTPP dyad was analyzed thoroughly in the previous chapter, the results and discussions on this complex are not repeated here. Therefore, only when a comparison is made, they will be referred to or appear, accordingly. The 5-6 isomer of this dyad is used here. The reason for choosing this isomer is that in the previous chapter, it was found that a different orientation of the endohedral unit does not cause a significant difference in the electronic structure of the two isomers. Therefore, it is sufficient for the purpose of this chapter to look at the results of one of them. Furthermore, the orientation of the encapsulated cluster in the fullerene cage of 5-6 dyad is identical to that of $Y_3N@C_{80}$_ZnTPP complex which makes the comparison of their results more sensible.

The $Y_3N@C_{80}$_ZnTPP molecule, depicted in figure 26, is a PF dyad possessing 161 atoms and 954 electrons. The center-to-center distance of the endohedral fullerene and the porphyrin moiety in the optimized complex is 7.66 Å. The trimetallic nitride endohedral fullerene employed as the acceptor moiety in this dyad is anticipated to bring along the advantages of this class of compounds for this complex. The results for this construct will be compared with the

$Sc_3N@C_{80}$_ZnTPP dyads', in which $Sc_3N@C_{80}$ plays the role of the acceptor, searching for the effect of having different acceptors.

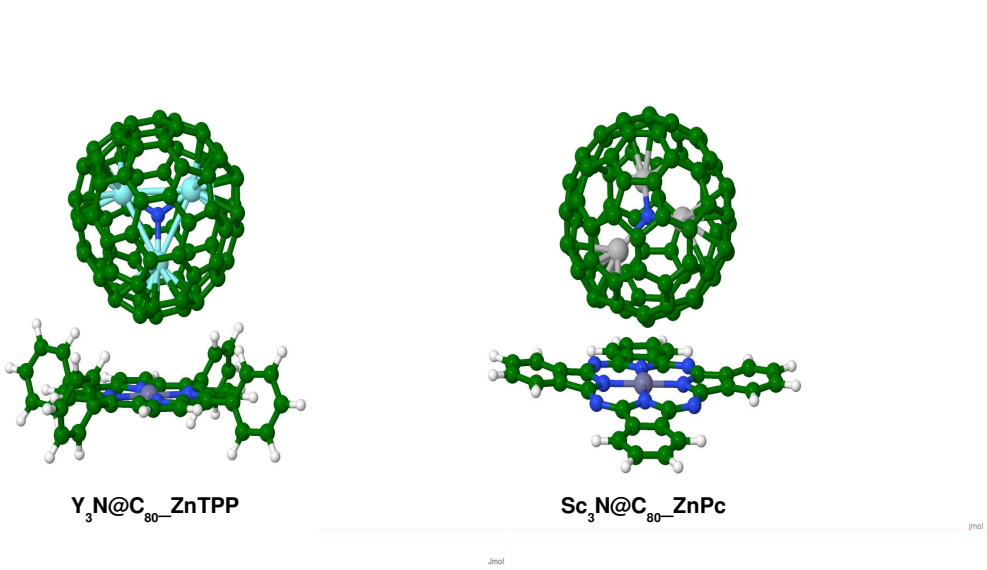

Figure 26. The pictures of $Y_3N@C_{80}$_ZnTPP and $Sc_3N@C_{80}$_ZnPc complexes.

The $Sc_3N@C_{80}$_ZnPc molecule is composed of 141 atoms and 844 electrons. The structure of this complex, as displayed in figure 26, was obtained by placing the two components in co-facial geometry. Then, the total energy of the system was computed as a function of the donor-acceptor surface-to-surface distance in increments of 0.3 Å. Later on the four lowest energy configurations were picked and the search for the most stable structure was continued by testing more points in between these four points. This energy scan, shown in figure 27(the middle panel), was obtained using the DFT approximations that include description of the van der Waals interactions. Energy vs. distance plot where the dispersion energy is not included is also provided in figure 27(the top panel). The contribution of the dispersion energy (using Zero

approximation method) is -0.189686 Ha. The optimal distance turned out to be at 3.09 Å. All degrees of freedom were relaxed at this optimal distance.

Furthermore, alteration of the ground state dipole moment of this molecule by varying the distance between the donor and the acceptor species were examined and plotted as illustrated in figure 27(the bottom panel). It shows that as the fragments of this dyad get farther away from each other, the corresponding dipole moment tends to zero. However, the calculated dipole moment in the optimal distance mentioned above (3.09 Å) is 0.32 Debye. We will compare the results for this complex with $Sc_3N@C_{80}$_ZnTPP dyads', in which ZnTPP is employed as the donor moiety to study the effect of having different donors.

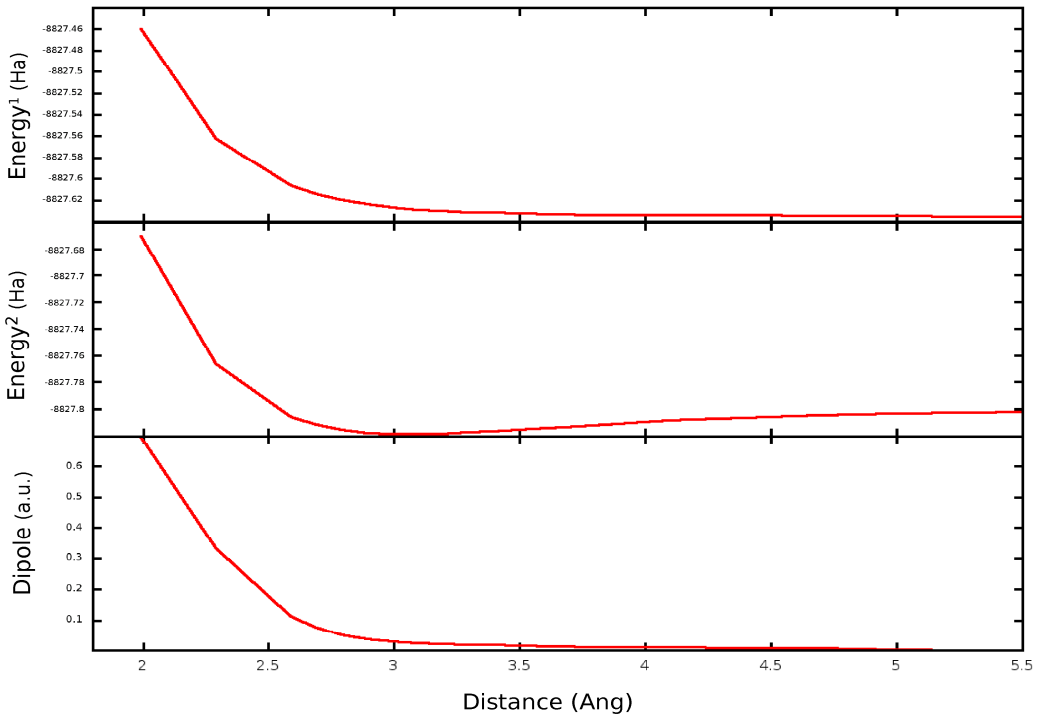

Figure 27. The ground state dipole moments and total energies as a function of donor-acceptor separation in $Sc_3N@C_{80}$_ZnPc dyad. In energy[1] values, the dispersion energy is not included while in energy[2] values, it is taken into account.

Table XI, displays the binding energies of all the complexes studied at this work. The applied definition for the calculation of these binding energies is as follows:

$$E_{BE}=E\ (complex)-\sum E\ (isolated\ (D\text{-}A)\ components)$$

Therefore, for a complex to have a stable structure, this value has to be negative. The table provides three different binding energies for each system. The total energy values used to calculate $E_{BE}(1)$ do not include the contribution of dispersion energy. However, to find the $E_{BE}(2)$ and $E_{BE}(3)$ values the Van der Waals interactions are considered and the dispersion energies are calculated employing Becke and Johnson (BJ) model and Zero approximation method for the $E_{BE}(2)$ and $E_{BE}(3)$, respectively. As was expected, the complexes exhibit stability when the dispersion energy contribution is taken into account whereas they are unstable if the van der Waals interactions are ignored.

Table XI. The binding energies of the four macromolecular dyads. In calculation of E_{BE} (1), the dispersion energy contribution is not considered while in $E_{BE}(2)$ and $E_{BE}(3)$, it is calculated using the Becke and Johnson (BJ) and Zero approximations, respectively.

System	E_{BE} (1) (eV)	E_{BE} (2) (eV)	E_{BE} (3) (eV)
$Sc_3N@C_{80}$_ZnTPP (5-6)	0.29	-0.57	-0.57
$Sc_3N@C_{80}$_ZnTPP (6-6)	0.26	-0.49	-0.51
$Y_3N@C_{80}$_ZnTPP	0.3	-0.32	-0.34
$Sc_3N@C_{80}$_ZnPc	0.305	-0.44	-0.43

The DFT calculated adiabatic/vertical ionization potential, adiabatic/vertical electron affinity, quasiparticle gap, exciton binding energy, ground state HOMO-LUMO gap and HOMO-LUMO excitation energy of these three systems are reported in Table XII.

Table XII. The DFT calculated IP, EA, quasiparticle gap, exciton binding energy, ground state H-L gap and H-L excitation energy of the three macromolecular complexes.

System	IP/vIP (eV)	EA/vEA (eV)	quasi-particle gap (eV)	exciton binding energy (eV)	gs_HOMO-LUMO gap/ HOMO-LUMO E_{ex} (eV)
$Sc_3N@C_{80}$_ZnTPP	6.12/6.13	----/2.50	3.63	1.47	1.17/2.16
$Y_3N@C_{80}$_ZnTPP	----/6.12	----/2.49	3.63	1.35	1.15/2.28
$Sc_3N@C_{80}$_ZnPc	----/6.12	2.66/2.62	3.5	1.36	1.14/2.14

The ionization potentials of the three complexes are almost the same. This result is anticipated for the first two since the same molecule (ZnTPP) is employed as the donor component in both. However, this remarkable proximity of their IP to that of $Sc_3N@C_{80}$_ZnPc suggests that replacing ZnTPP in $Sc_3N@C_{80}$_ZnTPP with ZnPc do not produce a significant change in the ground state electronic structure of this complex. A similar result can be drawn for the replacement of the acceptor part as the calculated EAs suggest it. However, as expected due to having the same acceptor part, the electron affinities of the first and the last constructs are very close differing by only 0.12 eV.

The calculated quasiparticle gaps for $Sc_3N@C_{80}$_ZnTPP and $Y_3N@C_{80}$_ZnTPP molecules are exactly the same differing by as much as 0.13 eV from $Sc_3N@C_{80}$_ZnPc dyad. However, the exciton binding energy for $Sc_3N@C_{80}$_ZnTPP is 0.12 eV/0.11 eV larger than that of $Y_3N@C_{80}$_ZnTPP/$Sc_3N@C_{80}$_ZnPc pair.

In order to study the shifts in energy levels upon complex formation, the ionization potential and electron affinity of the donors and acceptors in isolation and in complexes are given in Table XIII.

Table XIII. The DFT calculated ionization potentials (IPs) of the donors and electron affinities (EAs) of the acceptors in isolation and in complexes.

system	**$Sc_3N@C_{80}$**	**$Y_3N@C_{80}$**	**ZnTPP**	**ZnPc**	**$Sc_3N@C_{80}$_ZnTPP**	**$Y_3N@C_{80}$_ZnTPP**	**$Sc_3N@C_{80}$_ZnPc**
IP (eV)			6.29	6.34	6.12	6.12(vIP)	6.12(vIP)
EA (eV)	2.28	2.49			2.50	2.49(vEA)	2.66

The HOMO level of the Zn-porphyrin is raised by 0.17 eV in both $Sc_3N@C_{80}$_ZnTPP and $Y_3N@C_{80}$_ZnTPP complexes. Also, the HOMO orbital of the Zn-Phthalocyanine is shifted upward by 0.22 eV in $Sc_3N@C_{80}$_ZnPc dyad. On the other hand, the LUMO of the $Sc_3N@C_{80}$ fullerene has shifted in the same direction in both complexes employing it. It is lowered by 0.22 eV/0.38 eV in the $Sc_3N@C_{80}$_ZnTPP/$Sc_3N@C_{80}$_ZnPc dyad. No shift is observed for the LUMO orbital of the $Y_3N@C_{80}$ as it couples with ZnTPP.

The DFT calculated ground state dipole moment of $Y_3N@C_{80}$_ZnTPP and $Sc_3N@C_{80}$_ZnPc dyads turned out to be 0.49 and 0.32 Debye, respectively. As mentioned earlier, the ground state dipole moment may be due to ground state charge transfer or polarization. Comparing these two values with the ground state dipole moment of the $Sc_3N@C_{80}$_ZnTPP (0.66 Debye), it can be proposed that the presence of the ZnTPP in a complex causes a greater ground state charge transfer or polarization for that complex. Moreover, the DFT calculated excited triplet(mixed) state dipole moments for the HOMO-LUMO excitations are

24.89(24.91) Debye for the $Y_3N@C_{80}$_ZnTPP and 23.33(23.51) Debye for the $Sc_3N@C_{80}$_ZnPc dyad.

Figures 28 and 29, show the ground state density of states (DOS) of the two supramolecular complexes $Y_3N@C_{80}$_ZnTPP and $Sc_3N@C_{80}$_ZnPc as projected on their corresponding fragments.

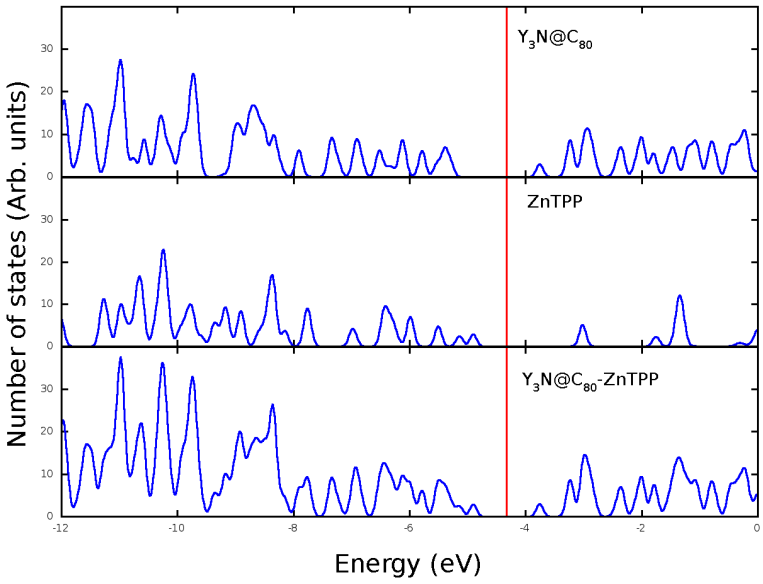

Figure 28. The total ground state density of states of $Y_3N@C_{80}$_ZnTPP dyad, projected on its components.

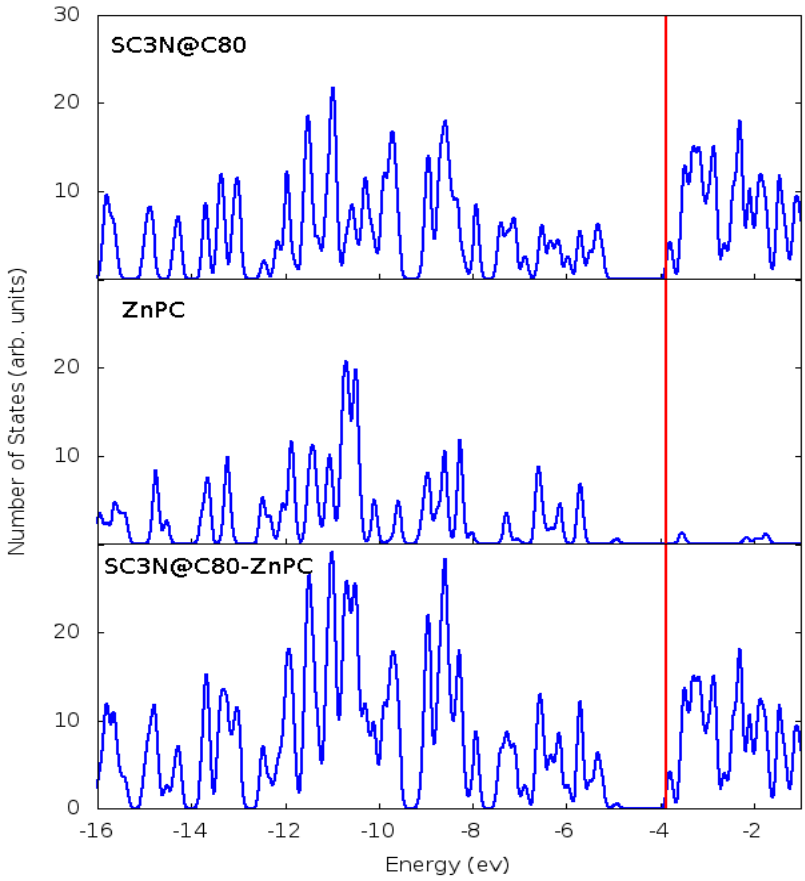

Figure 29. The total ground state density of states of $Sc_3N@C_{80}$_ZnPc dyad, projected on its components.

In both of these complexes the HOMO orbital is localized on the donor component (ZnTPP for the $Y_3N@C_{80}$_ZnTPP complex and ZnPc for the $Sc_3N@C_{80}$_ZnPc dyad) and the LUMO orbital sits on the acceptor part ($Y_3N@C_{80}$ for $Y_3N@C_{80}$_ZnTPP construct and $Sc_3N@C_{80}$ for the $Sc_3N@C_{80}$_ZnPc pair). Therefore, the HOMO-LUMO transitions correspond to charge transfer excited states. This is similar to the results obtained earlier for $Sc_3N@C_{80}$_ZnTPP complex. Furthermore, due to the presence of the trimetallic nitride endohedral fullerenes, they possess several low-lying closely spaced unoccupied molecular

orbitals above their LUMO level which is again a property already observed for the $Sc_3N@C_{80}$_ZnTPP system.

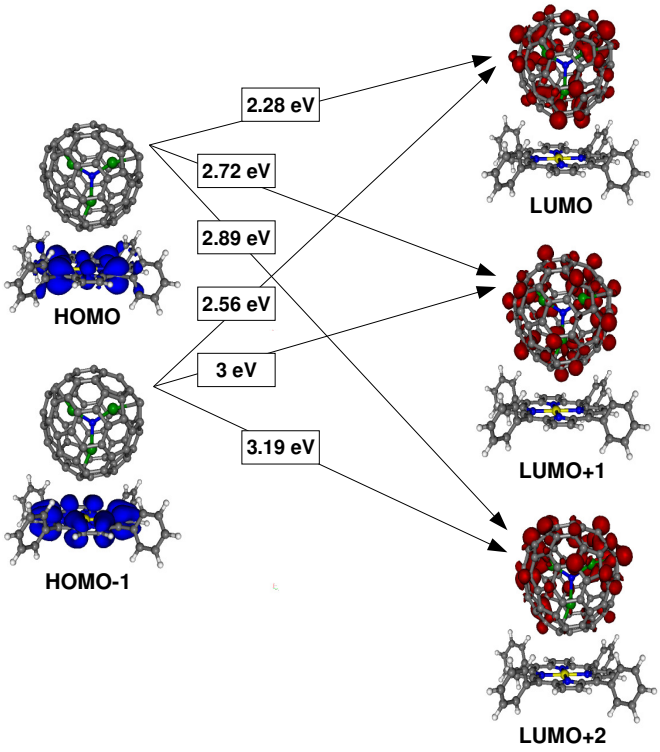

Figure 30. The lowest few charge transfer excitation energies in $Y_3N@C_{80}$_ZnTPP dyad.

A few low-lying charge transfer excitations of the $Y_3N@C_{80}$_ZnTPP dyad are represented schematically in figure 30. The left side of the figure displays the HOMO and HOMO-1 orbitals of this complex localized on the donor component and the right side shows the three lowest unoccupied molecular orbitals of $Y_3N@C_{80}$_ZnTPP molecule (LUMO, LUMO+1 and LUMO+2 orbitals), localized on the acceptor moiety. Since the orbitals are localized on their corresponding donor/acceptor components all of these transitions represent CT excited states. This is exactly what was obtained for the $Sc_3N@C_{80}$-ZnTPP complex. However, the value of the lowest CT

excitation energy has improved slightly for the $Y_3N@C_{80}$_ZnTPP pair. It is 2.16 eV for the $Sc_3N@C_{80}$_ZnTPP while it turns out to be 2.28 eV for the $Y_3N@C_{80}$_ZnTPP dyad. Therefore, replacing $Sc_3N@C_{80}$ by $Y_3N@C_{80}$ in $Sc_3N@C_{80}$_ZnTPP increases the lowest CT excitation energy by 0.12 eV.

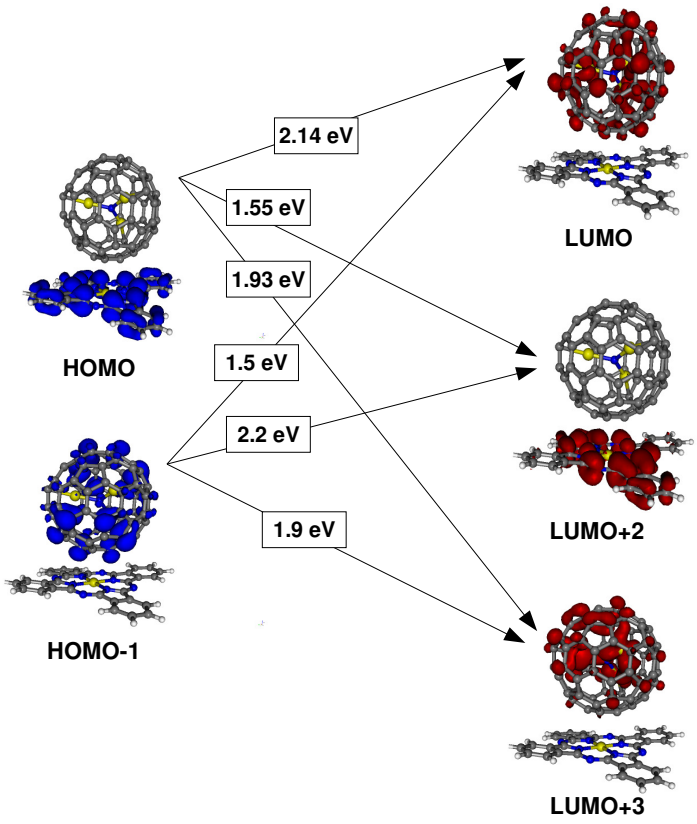

Figure 31. The lowest few excitation energies in $Sc_3@C_{80}$_ZnPc complex.

A few low-lying excitations of the $Sc_3N@C_{80}$_ZnPc complex are shown in figure 31. As the plots show, not all of these transitions between orbitals close to the Fermi level correspond to CT excited state transitions. For example, HOMO to LUMO+2 or HOMO-1 to LUMO transitions are local excitations. This is a behavior different from what the $Sc_3N@C_{80}$_ZnTPP

molecule demonstrates. In addition, the lowest CT excited state energy (occurring for HOMO to LUMO+3 transition), has decreased from 2.16 eV in $Sc_3N@C_{80}$_ZnTPP to 1.93 eV in $Sc_3N@C_{80}$_ZnPc construct. Thus, replacing ZnTPP by ZnPc in $Sc_3N@C_{80}$_ZnTPP decreases the lowest CT excitation energy by 0.23 eV.

Table XIV. A few excitation energies for the three macromolecular dyads. The energies of the triplet states are given in parentheses. All energies are in eV.

Transition	**$Sc_3N@C_{80}$_ZnTPP Singlet (triplet) State E_{ex} (eV)**	**$Y_3N@C_{80}$_ZnTPP Singlet (triplet) State E_{ex} (eV)**	**$Sc_3N@C_{80}$_ZnPc Singlet (triplet) State E_{ex} (eV)**
HOMO → LUMO	**2.16** (2.15)	**2.28**(2.28)	2.14(2.12)
HOMO → LUMO+1	2.51 (2.5)	2.72(2.69)	1.55(1.37)**
HOMO → LUMO+2	2.48 (2.47)	2.89(2.88)	1.55(1.31)*
HOMO → LUMO+3	2.46 (2.43)	2.49(2.38)	**1.93**(1.82)
HOMO → LUMO+4	2.96 (2.96)	2.05(1.83)*	1.88(1.75)**
HOMO → LUMO+5	2.87 (2.86)	2.03(1.83)*	**2.47**(2.41)
HOMO-1 → LUMO	2.3 (2.28)	2.56(2.56)	1.51(1.46)*
HOMO-1 → LUMO+1	2.65 (2.63)	3(2.97)	2.34**
HOMO-1 → LUMO+2	2.62 (2.61)	**3.19**(3.18)	2.2(2.19)
HOMO-1 → LUMO+3	2.61 (2.58)	2.72(2.64)	1.9(1.87)*
HOMO-1 → LUMO+4	**3.1** (3.08)	2.25(2.09)*	1.9(1.87)**
HOMO-1 → LUMO+5	3.02 (3.00)	2.23(2.09)*	1.95(1.88)*
HOMO-2 → LUMO	1.52 (1.48)*	1.59(1.54)*	1.6(1.55)*
HOMO-2 → LUMO+1	1.87 (1.84)*	2.1(2.01)*	2.19(2.16)**
HOMO-2 → LUMO+2	1.88 (1.85)*	2.15(2.1)*	2.46(2.44)
HOMO-2 → LUMO+3	1.95 (1.89)*	2.16(2.11)*	1.99(1.94)*
HOMO-2 → LUMO+4	2.19 (2.15)*		2(1.94)**
HOMO-2 → LUMO+5	2.19 (2.15)*		2.03(1.98)*

The excited state energies of the three dyads are given in Table XIV. Both the singlet and triplet excited state energies of the single particle excitations are reported. The singlet excited state energies are calculated using the Ziegler et al. formula, described earlier. In the table, transitions that are corresponding to the local excitations (charge transfer on the same

component) are indicated with an asterisk and transitions that are not purely charge transfer ones with non-zero overlap between the hole and the particle orbitals are displayed with two asterisks (These transitions are called partial CT excitations). It is emphasized that these calculations are done in gas phase ignoring the effects of solvents and ionic relaxations upon excitation.

The DFT calculated CT excitation energies lie within a range of 2.16 eV-3.1 eV for the $Sc_3N@C_{80}$_ZnTPP, 2.28 eV-3.19 eV for the $Y_3N@C_{80}$_ZnTPP and 1.93 eV-2.47 eV for the $Sc_3N@C_{80}$_ZnPc molecule.

To sum up, three different donor-acceptor pairs ($Sc_3N@C_{80}$_ZnTPP, $Y_3N@C_{80}$_ZnTPP and $Sc_3N@C_{80}$_ZnPc) were studied and various properties of them were analyzed and compared. The donors and acceptors were chosen from already proved promising candidates for utilization in OPVs. The goal was to investigate the effect of changing the donor or the acceptor component on the ground state and excited state electronic structure of the $Sc_3N@C_{80}$_ZnTPP compound. Employment of trimetallic nitride endohedral fullerenes as acceptor moiety produced a good number of low-lying closely spaced unoccupied molecular orbitals above the LUMO level for these dyads in ground state. The close calculated IPs and EAs for all the three complexes suggested that replacing either the acceptor component ($Sc_3N@C_{80}$ by $Y_3N@C_{80}$) or the donor part (ZnTPP by ZnPc) in $Sc_3N@C_{80}$_ZnTPP does not change the ground state electronic structure of this molecule. It was also found that the presence of the ZnTPP in the complexes gives rise to a more pronounced charge transfer or polarization in the ground state. The transitions corresponding to the lowest excitations demonstrate similar behaviors for the $Sc_3N@C_{80}$_ZnTPP and $Y_3N@C_{80}$_ZnTPP while they are mostly different in $Sc_3N@C_{80}$_ZnPc dyad including a few local excitations. It was realized that the $Y_3N@C_{80}$_ZnTPP dyad builds the

largest excited state dipole moment for the HOMO-LUMO transition among the three studied pairs. Finally, it was discovered that replacing the $Sc_3N@C_{80}$ by $Y_3N@C_{80}$ in $Sc_3N@C_{80}$_ZnTPP construct improves the lowest CT excited state energy by as much as 0.12 eV while replacing the ZnTPP by ZnPc in $Sc_3N@C_{80}$_ZnTPP decreases the lowest CT excitation energy by 0.23 eV.

References

1. D. Wohrle and D. Meissner, Advanced Materials 3 (3), 129-138 (1991).
2. Wikipedia (http://en.wikipedia.org/)
3. M. Tao, Inorganic Photovoltaic Solar Cells: Silicon and Beyond, The Electrochemical Society (2008).
4. D. Chapin, C. Fuller and G. Pearson, Journal of Applied Physics 25 (1954).
5. R. W. Miles, G. Zoppi and L. Forbes, Materialstoday 10 (11), 20-27 (2007).
6. C. J. Brabec, V. Dyakonov, J. Parisi and N. S. Sariciftci, Organic Photovoltaics: concepts and realizations. (Springer, Berlin; New York, 2003).
7. H. Hoppe and N. S. Sariciftci, Journal of Materials Research 19 (7), 1924-1945 (2004).
8. S. Gunes, H. Neugebauer and N. S. Sariciftci, Chemical Reviews 107 (4), 1324-1338 (2007).
9. L. M. Popescu, PhD thesis work done in the research group Molecular Electronics of the Zernike Institute for Advanced Materials at the University of Groningen, the Netherlands (2008).
10. M. F. Durstock, R. R. Smith, A. P. Smith, B. E. Taylor and L. Y. Chiang, Organic Solar Cells from Functionalized Donor-Acceptor Molecules, Wright state University.
11. I. D. Parker, Advanced Photonics Materials for Information Technology, 2144, 51-64 (1994).
12. C. J. Brabec, A. Cravino, D. Meissner, N.S. Sariciftci, T. Formherz, M. Minse, L. Sanchez, J. C. Hummelen, Advanced Functional Materials.
13. T. Baruah, M. Olguin and R. R. Zope, The Journal of Chemical Physics 137 (8), 084316-084316 (2012).
14. M. Olguin, R. R. Zope and T. Baruah, The Journal of Chemical Physics 138 (7), 074306-074306 (2013).
15. D. Gust, T. A. Moore and A. L. Moore, Accounts of Chemical Research 42 (12), 1890-1898 (2009).
16. T. Baruah and M. R. Pederson, Journal of Chemical Theory and Computation 5 (4), 834-843 (2009).
17. M. Olguin, L. Basurto, R. R. Zope and T. Baruah, the Journal of Chemical Physics 140 (20), 204309-204309 (2014).
18. B. P. Rand, D. P. Burk and S. R. Forrest, Physical Review B 75(11), (2007).
19. R. S. Mulliken, Journal of Physical Chemistry 56, 801 (1952).
20. R. R. Zope, M. Olguin and T. Baruah, The Journal of Chemical Physics 137 (8), 084317-084317 (2012).

21. M. Linares, D. Beljonne, J. Cornil, K. Lancaster, J. L. Bredas, S. Verlaak, A. Mityashin, P. Heremans, A. Fuchs, C. Lennartz, J. Ide, R. Mereau, P. Aurel, L. Ducasse and F. Castel, Journal of Physical Chemistry C 114(7), 3215-3224 (2010).

22. S. Wolfrum, J. R. Pinzon, A. Molina-Ontoria, A. Gouloumis, N. Martin, L. Echegoyen and D. M. Guldi, Chemical Communications 47 (8), 2270-2272 (2009).

23. J. M. Campanera, C. Bo, M. M. Olmstead, A. L. Balch and J. M. Poblet, Journal of Physical Chemistry A 106 (51), 12356-12364 (2002).

24. C. M. Cardona, A. Kitaygorodskiy and L. Echegoyen, Journal of the American Chemical Society 127 (29), 10448-10453 (2005).

25. D. M. Rivera-Nazario, J. R. Pinzon, S. Stevenson and L. A. Echegoyen, Journal of Physical Organic Chemistry 26 (2), 194-205 (2013).

26. J. R. Pinzon, M. E. Plonska-Brzezinska, C. M. Cardona, A. J. Athans, S. S. Gayathri, D. M. Guldi, M. A. Herranz, N. Martin, T. Torres and L. Echegoyen, Angewandte Chemie-International Edition 47 (22), 4173-4176 (2008).

27. E. B. Lezzi, J. C. Duchamp, K. Harich, T. E. Glass, H. M. Lee, M. M. Olmstead, A. L. Balch and H. C. Dorn, Journal of the American Chemical Society 124 (4), 524-525 (2002).

28. M. G. Walter, A. B. Rudine and C. C. Wamser, Journal of Porphyrins and Phthalocyanines 14, 759-792 (2010).

29. R. B. Ross, C. M. Cardona,D. M. Guldi, S. G. Sankaranarayanan, M. O. Reese, N. Kopidakis, J. Peet, B. Walker, G. C. Bazan, E. V. Keuren, B. C. Holloway and M. Drees, Nature Materials 8 (3), 208-212 (2009).

30. Y. Liang and L. Feng, Fullerenes, Nanotubes, and Carbon Nanostructures, 22 (1-3), 227-234 (2014).

31. Q. Wu and T. Van Voorhis, Physical Review A 72, 024502 (2005).

32. T. Ziegler, A. Rauk and E. J. Baerends, Theoretical Chemistry Accounts 43, 261 (1977).

33. M. Gouterman, Journal of Molecular Spectroscopy 6, 138 (1961).

34. M. Krause and L. Dunsch, ChemPhysChem 5 (9), 1445-1449 (2004).

35. H. M. Lee, M. M. Olmstead, E. Lezzi, J. C. Duchamp, H. C. Dorn and A. L. Balch, Journal of the American Chemical Society 124 (14), 3494-3495 (2002).

36. N. S. Sariciftci, L. Smilowitz, A. J. Heeger and F. Wudl, Science 258, 1474 (1992).

37. M. Maggini, G. Scorrano and M. Prato, Journal of the American Chemical Society 115, 9798 (1993).

38. D. Kuciauskas, S. Lin, G. R. Seely, A. L. Moore, T. A. Moore, D. Gust, T. Drovetskaya, C. A. Reed and P. D. W. Boyd, Journal of Physical Chemistry 100, 15926 (1996).

39. T. Drovetskaya, C. A. Reed and P. Boyd, Tetrahedron Letters 36, 7971 (1995).

40. N. Armaroli, G. Marconi, L. Echegoyen, J. -P. Bourgeois and F. Diederich, Chemistry-A European Journal 6, 1629 (2000).

41. F. Spanig, M. Ruppert, J. Dannhauser, A. Hirsch and D. M. Guldi, Journal of the American Chemical Society 131, 9378 (2009).

42. A. Kahnt, J. Karnbratt, L. J. Esdaile, M. Hutin, K. Sawada, H. L. Anderson and B. Albinsson, Journal of the American Chemical Society 133, 9863 (2011).

43. H. Imahori, K. Hagiwara, M. Aoki, T. Akiyama, S. Taniguchi, T. Okada, M. Shirakawa and Y. Sakata, Journal of the American Chemical society 118, 11771 (1996).

44. D. M. Guldi, A. Hirsch, M. Scheloske, E. Dietel, A. Troisi, F. Zerbetto and M. Prato, Chemistry-A European Journal 9, 4968 (2003).

Vita

Fatemeh Amerikheirabadi was born in Kerman, Iran. She did her undergraduate studies in physics, at the Islamic Azad University. She started her Masters' degree in physics on January, 2012 at the University of Texas at El Paso. In August of 2014, she finished her Masters' degree.

Permanent address: 3500 Sun Bowl Dr.
El Paso, TX, 79902

This thesis was typed by Fatemeh Amerikheirabadi